Journal of the Physical Society of Japan
Vol. 76, No. 8, August, 2007, 082001

Quantum Size Effects Induced Novel Properties in Two-Dimensional Electronic Systems: Pb Thin Films on Si(111)

Jin-Feng JIA, Shao-Chun LI, Yan-Feng ZHANG, and Qi-Kun XUE

Department of Physics, Tsinghua University, Beijing 100084, China
Institute of Physics, Chinese Academy of Sciences, Beijing 100080, China

(Received March 7, 2007; accepted May 8, 2007; published August 10, 2007)

Atomically flat metal ultrathin films grown on semiconductor substrates form a quasi-two-dimensional (2D) electronic system, which offers a great opportunity to explore novel properties induced by quantum size effects (QSE). In such a system, the motion of electrons in the film plane is essentially free, however, in the film normal direction it is confined, which leads to the quantized electronic states, i.e., quantum well states (QWS). The formation of QWS induces the redistribution of electrons and changes the electronic structure of the metal films and thus modifies their properties. By controlling the film thickness—the width of the confinement potential well, the QWS, together with the physical and chemical properties of the films can be engineered. In this article, we will summarize our recent studies on this problem in the Pb/Si(111) system, and discuss the perspectives in this area.

KEYWORDS: quantum well states, quantum size effects, Pb, growth behavior, properties, STM, ARPES
DOI: 10.1143/JPSJ.76.082001

1. Introduction

Nanomaterials usually exhibit novel properties that are remarkably different from their bulk counterparts and are of intense research interests in light of both fundamental science and technological applications. The underlying cornerstone for nanoscience and technology is quantum physics. Among many important problems in quantum mechanics, probably the one-dimensional (1D) "particle in a box", i.e., the confinement of electrons in a 1D square potential well with infinite walls, is the simplest and most well-known one. The 1D confinement results in formation of a set of discrete energy states, namely the quantum well states (QWS). The formation of the QWS, the so-called quantum size effects (QSE) depends strongly on the size of the systems and can dramatically regulate properties of such systems. Understanding the relationship between QSE and the resulted properties of nanomaterials are not only of great significance in basic research, but also very important for developing new functionalities and applications based on the existing materials. Despite of tremendous efforts along this line, such kind of research has been greatly limited by difficulties in atomic-level control of nanostructures and characterization of individual nanostructure, which is particularly true when the confinement takes place in more than one direction. The prepared nanostructures usually suffer from size fluctuation, resulting in not well-defined material properties, and hence the evidences for the QSE are often qualitative.

Atomically flat metal thin films on an appropriate substrate are one of the simplest real systems in terms of the above-mentioned quantum mechanics problem "particle in a box". In such a system, the motion of electrons perpendicular to the film surface is confined in the potential well formed between the vacuum level and substrate band gap (or wave vector-dependent relative gap for a metal substrate), as schematically illustrated in Fig. 1. Hence, the electrons are quantized into QWS[1–5] only in the film normal direction and behave as free electrons in the other two. By varying the film thickness, i.e., the width of the potential well, the electronic density of states (DOS) near the Fermi level (E_F) of the system could be modulated. If the film surface is atomically smooth in macroscopic scale, the QSE induced property modulation can be easily studied as a function of film thickness by most traditional macroscopic techniques.

The QWS has been already widely explored in metal films, such as Ag,[6] Mg,[7] Fe,[8] and other metals,[9] and the QSE on material properties, such as Hall effect,[10,11] superconductivity,[12,13] resistivity,[14] thermal stability,[15] have been reported. The QSE on growth behaviors has also been studied. In a fast scanning tunneling microscopy (STM) study on Ag/Ag(111),[16] the adatom island decay rates were found to be modulated by QSE. Another work using angle-resolved photoemission spectroscopy (ARPES) and X-ray photoelectron diffraction showed that pronounced QSE were only present in the Au films grown on Nb(100) at low temperature (LT), and the structure of the Au films changed to hexagonal close-packed (hcp and/or dhcp).[17]

The chemical reactivity of a surface, being closely related to the DOS at E_F [DOS(E_F)] and easily influenced by QSE, has also been investigated because of many important technological applications. Pronounced thickness-dependent variations in the oxidation rate were observed on Mg films on W(110) by comparing the initial oxidation rate of atomically flat Mg films of different thicknesses.[18] The changes in the decay length were proposed to explain the correlation between surface reactivity and QSE.[19]

The interaction between spin-polarized electrons and QWS, related to spin-dependent transport and oscillatory magnetic interlayer coupling, is another interesting topic.[20–23] By studying the QWS in non-magnetic metal films grown on magnetic metal substrates, not only the information on the thin metal films forming the well, but also the properties of interface and substrate could be obtained, since the QWS is very sensitive to the structure of interface and substrate. Some other QSE modified properties include surface plasma damping and dispersion,[24] optical absorption,[25] tunneling conductance[26] and so on.

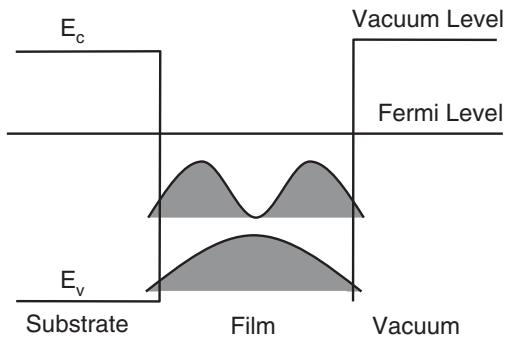

Fig. 1. Schematic of the one-dimensional square potential well structure with finite walls formed in a metal thin film grown on a semiconductor substrate.

To form QWS in a metal thin film, usually, a semiconductor substrate should be used where the band gap is necessary for establishing the confinement (see Fig. 1). Because of the very short Fermi electron wavelength (λ_F, in nanometer scale for most metals), an elaborate proof for the QSE requires atomically flat films with precise control of their thicknesses on a macroscopic scale, by which the property change can be detected by the traditional macroscopic methods. However, because of the lattice mismatch and different nature in chemical bonding, the growth of flat metal thin films with uniform thickness in macroscopic scale on a semiconductor surface is very difficult. Under the simplest picture of electronic wave interference (non-diffractive scattering), the metal film can be regarded as a Fabry-Perot interferometer. Thus, modulation of QWS in a metal film by its thickness (N) should cause an oscillatory variation of DOS (E_F), with a period defined as $\lambda_F/2a_0$ (a_0 is the interlayer spacing along the metal surface normal direction). A convincing demonstration of QSE is an oscillatory dependence of its properties on N. From this viewpoint, Pb(111) films are particularly unique for the study of QSE because λ_F in Pb is nearly four times of the interlayer spacing (a_0) along the (111) crystallographic direction ($\lambda_F \approx 4a_0$); only one atomic-layer variation in film thickness would cause a significant change in the electronic structure, and a shortest oscillation period of two monolayers (ML) is expected in the DOS as well as the properties so that the QSE would be easily observed (if the oscillation period is quite large, in order to establish a well-defined oscillation the films have to be very thick where the QSE might become insignificant).

Probably for this reason, many interesting results were obtained in the Pb/Si(111) system.[27–30] Non-diffractive scattering of electrons was directly observed in the wedge-shaped Pb islands on Si(111) by using STM,[4,5] its quantum origin was revealed by scanning tunneling spectroscopy (STS) measurement. Several groups observed that the stability of Pb islands depends on the thickness, magic and preferential heights of the islands were identified by their STM/STS measurements.[27] In the case of flat Pb films, ARPES studies revealed the significance of QSE on DOS(E_F)[31] and thermal stability of the Pb films,[11,32] and the stability was explained in terms of the electronic structure modulation by QWS. Quantum beating patterns in the thickness-dependent surface energy[32,33] were also observed, which, according to the simple picture mentioned above, should be a manifestation of the slight deviation from the perfect matching $\lambda_F = 4a_0$. Further studies on the thermal stability of Pb thin films showed the importance of interfacial structures,[34,35] which change the boundary conditions, and the resulted morphology changes can be easily understood by the phase accumulation model.[2,3]

The first definitive and quantitative demonstration of QSE on superconductivity in the Pb/Si(111) system was based on the atomically flat films.[36,37] By using a low temperature growth method to suppress the surface roughening due to the lattice and bonding mismatch, uniform Pb films in macroscopic scale, with precisely controlled thicknesses in terms of atomic layers, were prepared on Si(111)7 × 7 substrates. As a result, the quantum oscillations in superconducting transition temperature T_c were observed, which correlate perfectly with the confined electronic structure.[36] Other novel properties induced by QWS, such as double-layer growth,[29–31,38] selective strip-flow growth and growth rate modulation,[39] oscillating perpendicular upper critical field,[40] thermal expansion,[41] adhesion force,[42] local work function (LWF),[43] and surface diffusion barrier,[44] have also been observed. In this article, we would mainly summarize these recent results on Pb/Si(111) by our group. A more comprehensive review on the study of the QWS in metal thin films can be found elsewhere.[2,3]

2. Experimental Methods

The experiments were mainly performed in an Omicron STM-ARPES-MBE combination system under ultra-high vacuum (UHV; the base pressure is $\sim 5 \times 10^{-11}$ Torr). The Si(111) substrates were cleaned using the standard high-temperature flash procedure in the MBE chamber. High purity (99.999%) Pb was evaporated from a Knudsen cell, and the deposition rate was controlled to approximately 0.5 ML/min.[45] During the Pb deposition, the substrate was cooled down to ~145 K by liquid nitrogen flow and the pressure was controlled to lower than $\sim 5 \times 10^{-10}$ Torr. The film morphology were *in situ* monitored by reflection high-energy electron diffraction (RHEED) along the [1$\bar{1}$0] azimuth of the Si(111)-7 × 7 surfaces at glancing incidence angle with the electron beam energy of 12 KeV. After growth, the samples were slowly (5 K/min) warmed up to room temperature (RT) in order to anneal out morphological imperfections. As discussed in next section, this procedure ensures the films to be atomically flat and stable at RT for sample transfer from one place to another. Then, the samples were transferred from the MBE chamber to an analysis chamber, where an Omicron STM and an ARPES system were installed, allowing *in situ* characterization of the surface morphology and electronic structure. STM measurements were carried out at both RT and LT (~240 K) with a constant current (20 pA) mode. The photoemission spectra were collected by a GAMMADATA SCIENTA SES-2002 analyzer, with an energy resolution of 2 meV. For low temperature STM/STS and LWF measurements, a Unisoku low temperature STM-MBE system with a base pressure better than 1×10^{-10} Torr was used. In this system, the sample temperature can be cooled down to 2.2 K by liquid He while the data presented in this review were collected at 77 K.

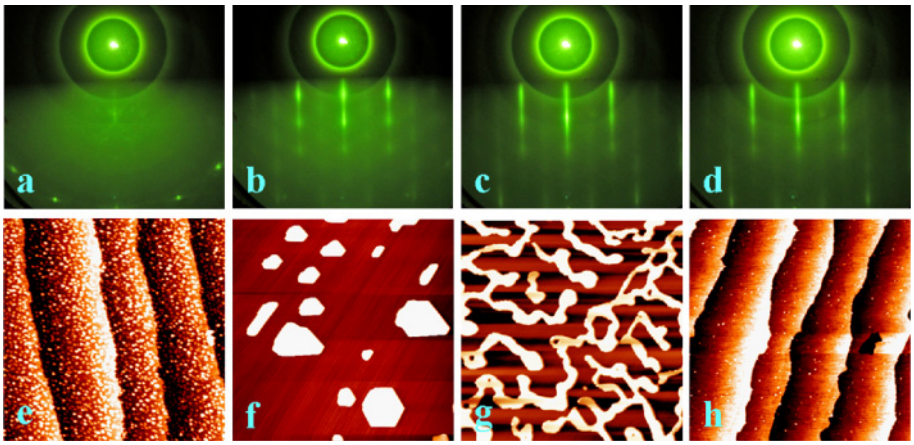

Fig. 2. (Color online) RHEED patterns [(a)–(d)] taken during Pb deposition on Si(111) substrate at 145 K, and the corresponding room temperature STM images [(e)–(h)]. The image size is 2000 × 2000 nm^2. Nominal thicknesses for the Pb films are 1, 3.5, 6, and 10 ML for (a), (b), (c), and (d), respectively.

The transport property measurements were carried out by using a Quantum Design Magnetic Property Measurement System (MPMS-5). To protect the Pb films from oxidation, several layers of Au were capped on them before taking out from the UHV chamber.

Note that, the thicknesses of the Pb films in the ARPES and superconductivity experiments are determined by fitting the phase accumulation model, with the wetting layer (3 ML) included, while in the experiments of selective strip-flow growth, thickness-dependent adatom surface diffusion, LWF and adhesion force thickness, where the Pb islands instead of the Pb films are explored, the thicknesses are directly measured from the top of the wetting layer in the STM images. Thus, there is a 3 ML (the thickness of the wetting layer) difference in the definitions of thicknesses for Pb films and islands.

3. Quantum Size Effects Induced Novel Growth Behaviors

3.1 Double-layer growth behaviors of Pb films

To suppress the Stranski–Krastanov growth of Pb on Si at RT and above, which is typical for a metal-on-semiconductor system where the lattice mismatch is usually large, a LT MBE growth of Pb films on Si(111) was employed to achieve an ideal two-dimensional (2D) system.[46] With this method, atomically flat Pb films in macroscopic scale could be prepared on several semiconductor substrates, whose stabilities depended strongly on the film thickness.[46–52] An "electronic growth" model was proposed to account for the intriguing growth behavior, where the QSE dominates in the magic stability of thin films.[53,54]

The upper panel in Fig. 2 displays the sequential RHEED patterns during Pb growth at the Si substrate temperature of 145 K. The 7× fractional diffraction streaks become weak after 1 ML Pb deposition [Fig. 2(a)] and disappear completely at 1.5 ML (not shown) because of the formation of featureless wetting layer. With increasing thickness, 1× like long dim streaks superimposed with bright spots appear [Fig. 2(b)], suggesting the formation of three-dimensional (3D) islands above the wetting layer. The spots, the fingerprint of the 3D islands, are interconnected gradually and evolve into long sharp streaks at ~6 ML [Fig. 2(c)]. Above 6 ML, the growth turns into layer-by-layer, as evidenced by the sharp 1 × 1 streaks. With further Pb deposition, there is no noticeable change in the RHEED patterns [Fig. 2(d)]. Although quantitative understanding needs more experiments, the limited atom diffusion at low temperature is the key factor for this intriguing 2D layer-by-layer growth.

Shown in the lower panel in Fig. 2 are the corresponding STM images recorded at RT. Below 1.5 ML, the deposited Pb atoms form a featureless wetting layer, consisting of small Pb clusters [Fig. 2(e)]. Many 3D flat-top islands are observed when the thickness is between 1.5 and 6 ML [Fig. 2(f)], corresponding to the streak-plus-spot RHEED pattern in Fig. 2(b). Surprisingly, while a uniform film in the thickness regime 6–10 ML is expected from the RHEED pattern in Fig. 2(c), the corresponding RT morphology exhibits interconnected islands [Fig. 2(g)]. The films only become stable at RT after the coverage increases to 10 ML, as shown by the STM image in Fig. 2(h). Hence, 10 ML can be identified as a critical thickness (or the smallest thickness) for the formation of stable films at RT.

The above morphology evolution (<10 ML) can be qualitatively explained by the "electronic growth" model. According to this model, the stability of a thin film is intimately related to the electronic contribution to the system energy, which mediates a long-range force, counteracting the unfavorable over-layer substrate interface energy.[53,54] The trade-off between the energy minimization by the long-range force and the energy punish from the thermal effects defines a "critical thickness" of 10 ML at RT.

Above 10 ML, the RT morphology of the films exhibits a double-layer structure (Fig. 3); while the 13 ML film shows an atomically smooth surface [Fig. 3(a)], the 14 ML film is actually composed of a flat 13 ML film plus 2 ML-high islands covering 50% of the surface area. Such double-layer structure appears again for the thicknesses of 16 ML, 18 and 20 ML. Since the quantized energy levels or the QWS of a film are unique to its thickness by the Bohr–Sommerfeld quantization rule,[2,3] we use photoemission spectroscopy to identify the magic stability or double-layer structure. Series ARPES spectra of the Pb films with atomically flat surface are displayed in Fig. 3(c). The sharp and intense peaks near the Fermi level correspond to the QWS peaks, while the broad and less intense peaks with a binding energy larger

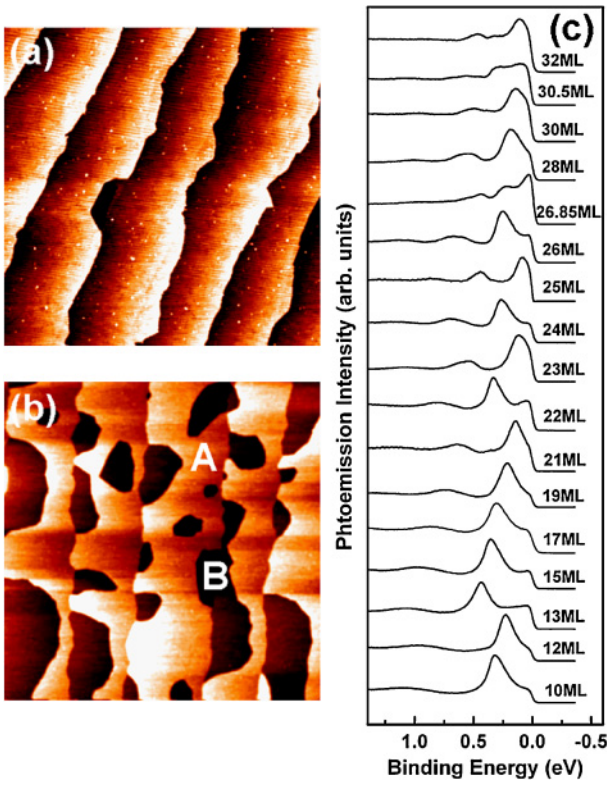

Fig. 3. (Color online) Room temperature STM images (2000×2000 nm^2) of the Pb films of 13 ML (a) and 14 ML (b). All stable films exhibit essentially the same morphology as shown in (a), and are (111) oriented. In (b), the letter "A" indicates the 2 ML high islands on top of the 13 ML film labeled with the letter "B". (c) Normal emission spectra measured at 110 K with the successive spectra graphically offset for clarity. Binding energy at 0.0 eV corresponds to the Fermi level.

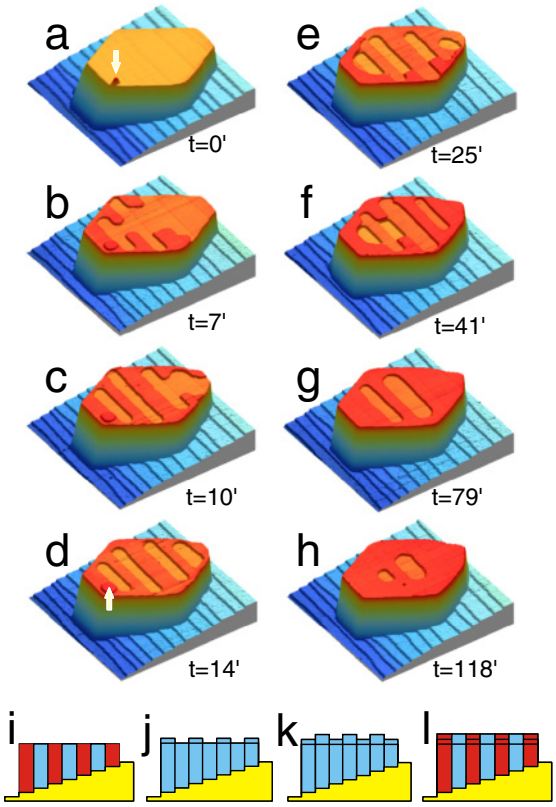

Fig. 4. (Color online) Snapshots of STM images (1000×1000 nm^2) recorded at room temperature showing the evolution of a Pb island on Si(111) after triggered by a voltage pulse of +5 V. (a) The original as grown Pb island after deposition. The thickness of Pb layers on top of each Si terrace increases successively from 4.5 to 7.3 nm. The arrow marks the position where the voltage pulse was applied. (b)–(d) QSE driven strip-flow growth turning odd-layer-number regions into even numbers of layers. (e)–(f) Double-layer growth taking place on the original even number layers. (g)–(h) Flat top recovery growth to reduce surface steps. (i)–(l) Side-view schematics showing the original island, selective strip-flow growth, double-layer strip growth and flat-top-recovery growth respectively. Gray indicates the QSE-favored even-layer-number regions, and dark the QSE-unfavored odd numbers of layers.

than 0.5 eV derives from the resonance states. Evidently, if a film is terminated with a complete layer, its spectra only show a single set of intense and sharp QWS peaks, as in the case of 10, 12, 13, 15, 17, 19, 21, 22, 23, or 24 ML. Deviations from the perfect integer layers will destroy the singularity of the QWS, as shown in the spectra of 26.85 and 30.5 ML films [Fig. 3(c)]. For the films with nominal thicknesses of 11, 14, 16, 18, and 20 ML where half of the surface is covered by 2 ML-high islands, the corresponding photoemission spectra exhibit a mixture of different sets of QWS peaks from the adjacent stable layers as shown before. Based on the measurements by both ARPES and STM, the observed double-layer growth is nothing but a consequence of QSE which favors formation of a film with minimized electronic energy. From these measurements, a turning point at 13 ML, where the stable thicknesses change from even layers (below 13 ML) to odd layers, was also identified. Above 21 ML, the growth proceeds basically via a layer-by-layer mode and atomically flat films with continuous layers could be obtained.[38)]

3.2 *Selective strip-flow growth on Pb islands and growth rate modulation*

If the coverage is controlled to less than about 3 ML and deposition is performed at RT, the Pb growth on Si(111) substrate proceeds in the Stranski–Krastanov mode, i.e., first wetting the Si substrate by ~2 ML followed by formation of Pb islands on top of the wetting layer. As shown in Fig. 4(a), the as-grown Pb islands usually display a flat-top wedge shape on the stepped substrate, covering about 10 steps with the thickness increasing from right to left. The side view of the wedged islands is schematically shown in Fig. 4(i). To initiate a new atomic layer to grow on top of the Pb wedge, voltage pulses up to ~10 V were applied from the STM tip to the position where the re-growth is expected to start. During the STM pulse manipulation, the feedback was kept active to avoid tip crash, and right after the manipulation, normal STM scanning was resumed to monitor the morphology evolution.

The interlayer spacing of Si (~3.12 Å) is comparable with Pb (~2.84 Å) in (111) direction, and thus the Pb wedge thickness varies consecutively in terms of atomic layers, i.e., both the even layered and odd layered regions exist, as marked by dark and gray in Fig. 4(i). The Pb island shown in Fig. 4(a), for example, contains number of layers continuously from 15 to 24. Due to the formation of QWS, the electronic structure, especially the DOS(E_F) of Pb films, changes periodically with a period of ~2 ML in terms of the position of the highest occupied (or lowest unoccupied)

QWS (see §4 for details), inducing higher total electrons' energy in odd layered regions than in even layered regions, as documented in last section. Therefore, the even layered regions are more stable than the odd layered ones in terms of the QSE. The electronic oscillation with thickness on Pb wedge was also investigated through STS measurement previously.[4,5] In the thickness regime where the QSE dominates over the classical step effect that induces the flat-top morphology, one more atomic layer are anticipated to be added to the odd layered regions to decrease the quantized electrons' energy and thus the total energy. However, to reach such a quantum lowest energy state (all regions on the Pb wedge are even layered), the kinetics barrier has to be overcome to reach the right growth pathway. While, in the thickness regime where the QSE is comparable with the classical step effect, the system is frustrated to satisfy both the electron energy and step energy at the same time.

The kinetics barrier can be overcome by the STM manipulation and massive atom transport is then initiated in a controllable manner, transforming the wedge morphology and swinging it back and forth between the two extreme states [Figs. 4(i) and 4(j)] favored by either effect. By applying a voltage pulse, one more atomic layer starts to grow spontaneously from where the pulse was applied, as marked by the arrow in Fig. 4(a), on only the odd layered regions and the even layered regions were left unchanged. Such kind of triggered growth is featured by strip-flow growth.[55] The strip-flow growth continued until the wedge transformed into the QSE minimized state, i.e., the Pb wedge with whole regions even layered, as shown by Figs. 4(d) and 4(j). After the strip-flow growth completed, the strip-top Pb wedge would recover the flat-top again by growth of the atomic layer onto the original unchanged even layered regions (image not shown). During the flat top morphology recovery, the surface step energy is decreased, while the quantum electrons are driven to a higher energy state.

The QSE driven strip-flow growth can dominate over the flat top recovery only if the kinetics barrier was overcome. By applying a second voltage pulse before the flat top recovery started, a double layer growth, driven by QSE, was triggered as shown in Figs. 4(e)–4(g), and Fig. 4(k).[55] Again, when left alone, the growth will ultimately proceed to restore the flat-top configuration [Figs. 4(g) and 4(h)]. As long as the thickness of the Pb wedge is increased to exceed ~26 ML (critical thickness), the transition from the QSE driven strip-flow growth to the classical growth,[56] wetting the wedge edge followed by vacancy island decay, took place, as shown in Fig. 5(a). On the other hand, the quantum beating pattern on the function of surface energy vs the thickness is also observable in real space when the thickness is decreased to about 17–18 ML. Figure 5(b) shows that the strip-flow growth takes place on the thicknesses of 16, 19, 21, and 23 atomic layers, while both 17 and 18 layered regions are not changed. It means that, at the thickness above 17–18 MLs, the even layered regions are stable, while at the thickness below 17–18, the odd layered regions are more stable, indicating the QSE on these two regions are not strong enough to dominate over the classical step effects, and in agreement with the previous report.[15,32]

The competing between the QSE and CSE can be more

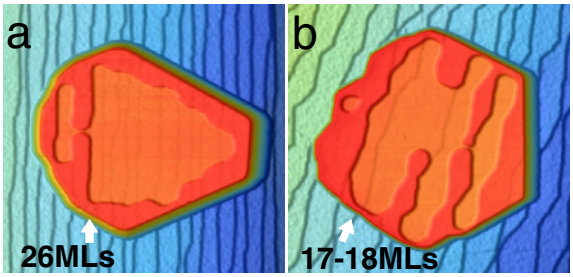

Fig. 5. (Color online) (a) STM image ($1000 \times 1000\,nm^2$) illustrating the quantum-classical growth transition, the white arrow indicates the critical thickness of 26 ML. (b) STM image ($1300 \times 1300\,nm^2$) illustrating quantum beating in morphological dynamics, the arrow indicates the critical thicknesses of 17 and 18 ML. The thickness increases from left to right for Pb islands in both (a) and (b).

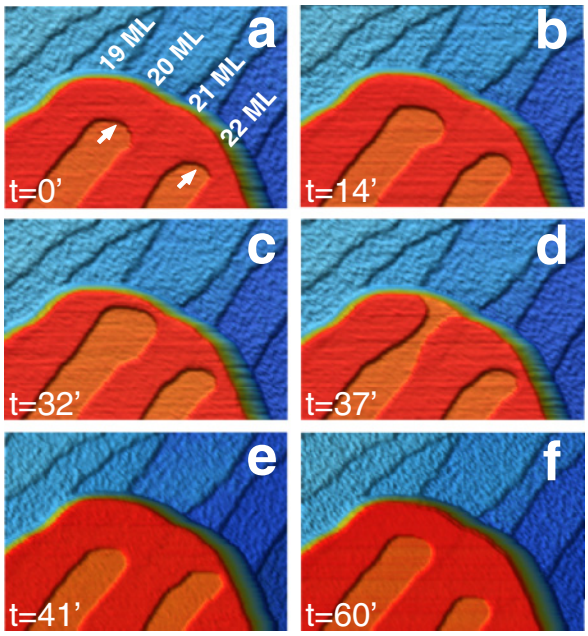

Fig. 6. (Color online) STM images showing the intra-layer diffusion alongside the growth front. The direction of the intra-layer diffusion is marked by arrows in (a). The size is $200 \times 300\,nm^2$. The wedge thicknesses of the original flat-top Pb wedge are marked in (a). (a) to (c) Diffusion from even layered regions to odd layered regions, (d) Diffusion from 20 ML to other regions is completed; (e) New Pb atoms jump up to the bare 20 ML region (d) and form an edge area; (e) to (f) diffusion from even layered to odd layered resumes.

clearly seen from the intra-layer diffusion of the growing atomic layer. Figure 6 shows a part of Pb wedge which are triggered by a voltage pulse of +7 V at ~240 K. Figure 6(a) shows the intermediate state when the strip-flow growth has not completed. Since the growth is triggered at low temperature, the growth rate is slow enough to capture the growth front evolution with time. The intra-layer diffusion from even layered region to odd layered regions took place at the places marked by arrows in Fig. 6(a). After 35 min, all the Pb atoms on 20 ML layer diffused to neighbouring layers [Figs. 6(b)–6(d)]. Evidently, the classical step effect would drive the growth front to circular shape to decrease the total step length, while the QSE would confine the growth front exactly alongside the substrate steps. Since the QSE dominate over CSE at this thickness regime, the net

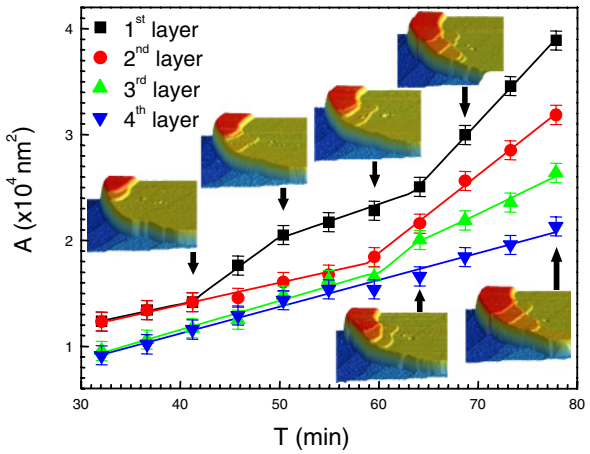

Fig. 7. (Color online) Time evolution of four stacked Pb layers created by a voltage pulse of +7 V applied at $t = 0'$ to the STM tip. The STM manipulation and scan were performed at ~240 K. The 1st, 2nd, 3rd, and 4th layers are marked from bottom to up. Insets show the corresponding STM images ($300 \times 230\,\mathrm{nm}^2$). The thickness of the original Pb island increases from right to left.

diffusion took place from the even layered to odd layered regions.

Diffusion rate is also confirmed to oscillate up and down with the thickness, indicating that it is also mediated by QSE. Figure 7 shows the time evolution of the growth areas of four stacked atomic layers alongside the Pb wedge edge at ~240 K. Two different slopes (growth rates) can be easily distinguished, with the higher rates (the first layer at 41 and 64 min) took place on the odd layered regions and the slower (the first layer at 50 min and the third layer at 64 min) on the even layered regions. The diffusion rate oscillation provides another evidence to rule out the strain effect, and thus confirm the QSE is the main driving force on the triggered growth.

In this part, the STM voltage pulses are used to trigger the new atomic layer growth on top of the Pb wedge. The morphology evolution of the new atomic layer is driven by QSE and CSE alternately for different thickness regime. Additionally, the kinetic barrier has to be overcome to initiate the growth, which has been realized by applying a STM voltage pulse. The growth rate and the intra layer diffusion are also confirmed to be mediated by QSE.[39)]

3.3 Thickness-dependent adatom surface diffusion

QSE on epitaxial growth of ultrathin metal films, in particular ultrathin Pb films on Si(111) substrate, has attracted considerable attention recently.[4,5,27,28,36,37,53–55,57)] These studies have greatly enriched our fundamental understanding of epitaxial growth of thin films by revealing many new insights, since quantum effects are generally ignored in the conventional view of epitaxial growth. The study of QSE in this aspect will certainly also impact on fabrication of metallic nanostructures and nanodevices.

Epitaxial growth process is generally controlled by the competition between thermodynamic and kinetic factors. One may expect that for very thin metal films, QSE will affect not only growth thermodynamics but also kinetics. However, the existing studies of QSE on growth of ultrathin films have focused mostly on growth thermodynamics,[15,30,32,38,56)] e.g., the energetics and film stability. In addition to the intriguing bi-layer growth discussed in the last section, here, we demonstrate by experiments and simulations the QSE on surface diffusion coefficient, a fundamental parameter of growth kinetics, through the measurement of island nucleation density at the early stage of growth.

Surface diffusion is the most fundamental kinetic factor in controlling the epitaxial growth process, and hence a subject of extensive studies.[58)] On the surface of a very thick metal film, surface diffusion coefficient is generally a constant, characteristic of a given surface. It is well known that QSE has a profound impact on the stability of ultrathin metal films.[4,5,15,27,28,30,32,36–38,53–57)] Intuitively, however, it is difficult to envision how QSE would change surface diffusion.

One way to derive surface diffusion coefficient is by measuring island nucleation density at the early stage of epitaxial growth in the sub-monolayer regime, using STM.[59,60)] We have applied this method to explore the QSE on surface diffusion, using nucleation/growth of Fe islands on Pb thin films of different thickness as a model system of study. By counting Fe island density under the same conditions and comparing the kinetic Monte Carlo (kMC) simulations with the experimentally measured island densities, we could deduce the surface diffusion barrier on a 21 and 26 ML Pb film to be 204 ± 5 and 187 ± 5 meV, respectively. As a further illustration, we also carried out growth experiments on wedged Pb films of different layer thickness, where the density of Fe islands exhibits an oscillatory behavior, being consistently higher on the odd-layer film than on the even-layer film.

Fe islands were grown on top of Pb films at both LT and RT by evaporating Fe from a tantalum boat by direct current heating. The deposition rate was approximately 0.08 ML/min. *In situ* STM measurements were conducted at RT.

Because of the low solubility and large surface energy difference between Fe and Pb, the Fe islands nucleate and grow into a conglobated shape at both LT and RT. At a very low coverage, the islands have an average diameter of 2–2.5 nm and an average height of 0.25–0.35 nm. With increasing coverage, the islands grow into a fractal shape with increasing ramification and their height gradually saturating at ~0.6 nm.

Figures 8(a) and 8(b) show the STM images of Fe islands grown on atomically flat 21 and 26 ML Pb films, respectively, with the same nominal Fe coverage of 0.24 ML. In both images, there are smaller islands decorating the step edges and concentrating at some local corrugated surface regions, indicating nucleation is more favorable at those locations. But overall, it is evident that the average island density (number of islands per surface area) is notably higher on the 21 ML Pb film [Fig. 8(a)] than on the 26 ML Pb film [Fig. 8(b)], while the average island size is smaller in the former than in the latter. Both images have the same resolution and size of $200 \times 200\,\mathrm{nm}^2$.

To obtain a statistical average of island density, we have selectively counted the islands in the open flat (strain-free) surface areas from 20–25 STM images as Figs. 8(a) and 8(b), in a total number of 350–450 islands. Figure 8(c) shows the counting results of island density on both the 21 and 26 ML Pb films for comparison. The average island density ($\sim 1.53 \times 10^{11}\,\mathrm{cm}^{-2}$) on the 21 ML film is found to

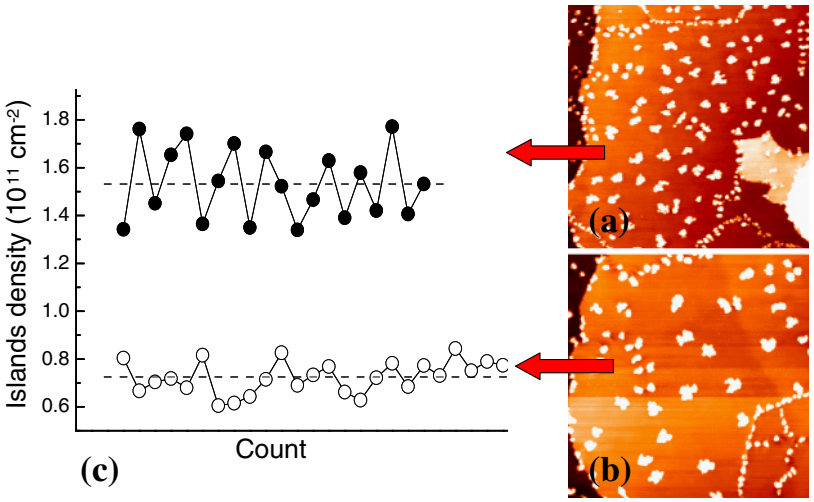

Fig. 8. (Color online) STM images of Fe islands grown at LT on (a) 21 ML and (b) 26 ML Pb film, respectively, up to the same coverage of 0.24 ML. Both images are $200 \times 200\,\text{nm}^2$ taken with a tip bias of -2.67 V and tunneling current of 20 pA. (c) Counted Fe island density on 21 ML (solid circle) and 26 ML (open circle) Pb film, corresponding to (a) and (b), respectively.

be nearly two times of that ($\sim 0.73 \times 10^{11}\,\text{cm}^{-2}$) on the 26 ML film. We have also checked the average island size on the two films; the island size on the 21 ML film ($\sim 54\,\text{nm}^2$) is about one-half of that ($93\,\text{nm}^2$) on the 26 ML film. Given the same island height (~ 0.67 nm), this is consistent with the same nominal Fe coverage of ~ 0.24 ML on the two films.

The most reasonable explanation for the observed island density difference is a thickness-dependent surface diffusion coefficient due to the QSE, since other growth parameters, the temperature and the deposition flux, are kept the same. According to the classical nucleation theory of epitaxial growth,[59–61] the island density (N) depends on deposition rate (F) and surface diffusion coefficient (D) in the submonolayer regime. For isotropic surface diffusion and the critical nucleus size of one, the island density follows the scaling relation of $N \propto (F/D)^{1/3}$.[59–61] Therefore, the different island density on the 21 and 26 ML film is mainly originated from the different surface diffusion coefficient on the two film surfaces. Assuming the prefactor of attempt frequency for surface diffusion is the same, we derive the difference of surface diffusion energy barrier on the two surfaces to be in the range of ~ 28 meV, using the deposition temperature of 150 K.

The above experiments provide not only a direct proof of QSE on surface diffusion but also a quantitative measure of diffusion barrier difference induced by QSE. Moreover, it has been demonstrated before[59,60] that one can obtain the absolute diffusion barriers by matching the island densities from kMC simulations to the experimental results. Normally, this is done by simulating island density as a function of temperature (i.e., an Arrhenius plot) on a given surface of single diffusion barrier. Here, however, we will instead simulate island density as a function of diffusion barrier at the given deposition temperature, since the experiments were performed under identical conditions with different diffusion barriers on different surfaces.

We used a solid-on-solid model and a simulation cell of 164×142 hexagonal grid ($100 \times 100\,\text{nm}^2$). The choice of using a hexagonal cell was made based on recent first-principles calculations[62,63] which showed that the adatom surface diffusion on Pb(111) film surface takes effectively a hexagonal pathway with the fcc and hcp hollow sites being respectively the minimum-energy and saddle point. In accordance with the experiments, the simulations were carried out at 150 K, using a deposition rate of 0.08 ML/min up to a total coverage of 0.24 ML. The attempt frequency for adatom diffusion was set at $kT/h = 3.12 \times 10^{12}\,\text{s}^{-1}$. For each given diffusion barrier, simulations were repeated 10 times to obtain a statistical average island density.

Figure 9 shows the simulated island density as a function of surface diffusion barrier in a semi-log plot. The solid line is a linear fit to the simulation data, as predicted by the classical mean-field nucleation theory.[59–61] The data appears to be slightly sublinear, which is caused by island coalescence at higher densities that is not accounted for by classical mean-field theory. By matching the simulated island densities to the two experimentally measured values on the linear curve (see dashed lines in Fig. 9), we obtain the Fe surface diffusion barriers on the 21 and 26 ML Pb film to be respectively 204 ± 5 and 187 ± 5 meV, with a difference of 17 meV. This difference is a few meV smaller than the estimate (~ 28 meV) by the simple scaling of experimental densities, indicating that the simple mean-field scaling

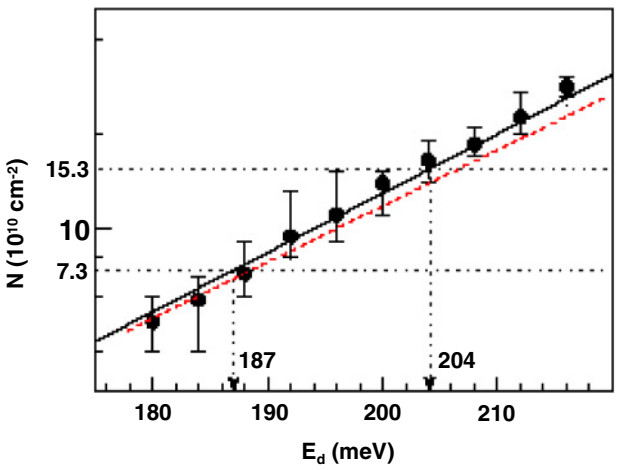

Fig. 9. (Color online) Island nucleation density (N) as a function of surface diffusion barrier (E_d), obtained from kMC simulations. The solid line is the linear fit to the 3D island data (solid dots). The two dotted horizontal lines mark the experimental densities, from which the surface diffusion barriers were derived as indicated on the x axis. For comparison, the dashed line is the fit to the 2D island data, which were not shown for better clarity.

of experimental densities would overestimate the barrier difference.

Comparing the solid line (3D island results) with the dashed line (2D island results) in Fig. 9, one sees that the dashed line has a slightly smaller slope. This is caused by the coalescence of laterally larger 2D islands at higher densities as shown by the simulations. But the overall difference between the 3D and 2D island simulations is small, indicating that the nucleation density is largely determined by the adatom–adatom collision rate, with the critical size of one, and less dependent of the shape that the island grows into. We note that in our analysis and simulation, we assumed critical nucleation size of one atom independent of film thickness. One can imagine that if QSE can strongly change the binding between adatoms and hence the critical size, then it may also induce oscillation in island density. This could be a very interesting subject for future studies.

We carried out also another set of experiments depositing Fe on wedged Pb films on a vicinal Si(111) substrate consisting of a staircase of steps, where Fe island will simultaneously nucleate on one flat surface of Pb film but of different underlying film thickness. This allows a direct comparison of island density in different surface regions, as illustrated in Fig. 10, which shows the STM image of ~0.08 ML nominal Fe deposition at RT on a wedged Pb island of varying thickness from 10 to 15 ML. The wedge Pb film has a flap top, so its thickness changes by one atomic layer when passing over a substrate step.

Evidently, the Fe island density displays an interesting odd–even oscillation, with higher densities on the surface region of the odd-layer film (e.g., 11 and 13 ML) than those of the even-layer film (e.g., 12 and 14 ML). Island counting on a number of such samples shows that the average island density on the odd-layer surface ($\sim 2.95 \times 10^{10}\,\mathrm{cm}^{-2}$) is ~55% higher than that on the even-layer surface ($\sim 2.03 \times 10^{10}\,\mathrm{cm}^{-2}$). Here, we exclude the two outmost layers, such as 10 and 15 ML in Fig. 10, on which the island density is much lower because deposited adatoms have diffused out of island edges.

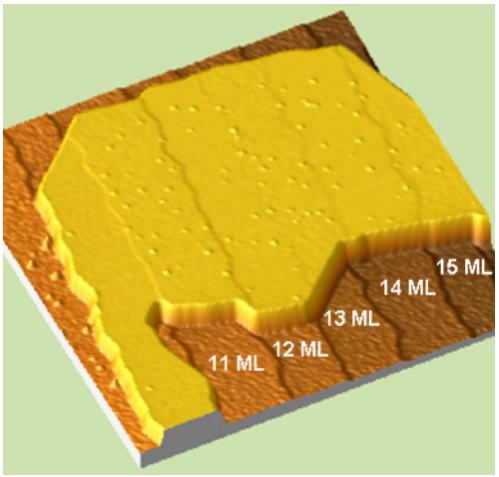

Fig. 10. (Color online) A $1000 \times 1000\,\mathrm{nm}^2$ STM image (acquired at a tip bias of −5.0 V and tunneling current of 20 pA) displays a density oscillation of Fe islands nucleated on a wedged Pb film at RT. The island density on the odd-layer films (11 and 13 ML) is notably higher than that on the even-layer films (12 and 14 ML).

This experiment has the advantage of uniform deposition rate and temperature than separate experiments to illustrate directly the film thickness dependent island densities. However, we found a quantitative derivation of diffusion barriers is difficult due to several other complications. First, many adatoms have diffused out of the wedged film. There are clearly denuded zones around the film edge and the final coverage is respectively ~0.024 and 0.016 on the odd- and even-layer films, which are much smaller the nominal deposition (~0.08 ML). As a result, mean-field theory counting the total deposited atoms is not applicable. Second, first-principles calculations[62,63] showed that in addition to diffusion barriers, QSE modulates the adatom binding energies. This causes a difference in adatom chemical potential in different surface regions, leading to non-uniform surface coverage, as seen in the observed final coverage differences in the different surface regions. This would in turn affect the island nucleation densities.

Nevertheless, if the island density oscillation were assumed to be solely caused by difference in surface diffusion, we could roughly estimate the average surface diffusion barriers on the odd-layer films is ~34 meV higher than those on the even-layer films, using the classical nucleation scaling relation and neglecting the difference among the odd- or even-layer films, i.e., 11 vs 13 ML or 12 vs 14 ML. So, the two sets of experiments seemed to indicate that the QSE induced surface diffusion barrier difference is larger on thinner films (11 to 15 ML) than that on thicker films (21 vs 26 ML), which is consistent with one's physical intuition.

Several other recent experiments have also indicated indirectly the QSE on surface diffusion. For example, it has been found that the Pb island nucleation on top of a Pb mesa starts from the edge on a five-layer mesa but from the middle on a six-layer mesa,[64,65] and the growth rate of the overlayer depends on mesa thickness.[39] These phenomena, however, involve heavily other growth parameters, in particular the mesa edge or step edge barriers, which makes the determination of diffusion barriers very difficult. In contrast, our experiments here isolate the surface diffusion barrier as the most direct kinetic parameter to be quantitatively determined. On the other hand, first-principles calculations have indeed shown a large QSE on Pb adatom diffusion barriers on Pb(111) film.[64,65] Future calculations may be done for Fe adatom diffusion on Pb(111) to be compared with our experiments.

We have tried to account for these complications by performing kMC simulations. In this case, we divided the 400×400 simulation cell into two equal 200×400 subcells of different surface diffusion barrier: the center cell with a diffusion barrier of 168.5 meV and the outer cell with 212.5, whose average was set the same as that on the 21 and 26 ML film with a difference of 34 meV. We used the periodic boundary condition in the x-direction to mimic the two center regions of the wedged film. In the y-direction, we set the 75% adatoms to disappear at the boundary and 25% being reflected back, which will amount to the final average coverage of 0.02 ML after 0.08 ML nominal deposition. Figure 11 shows the simulation result at $T = 300$ K. The resulting island density is respectively $\sim 2 \times 10^{10}$ and $\sim 3 \times 10^{10}\,\mathrm{cm}^{-2}$.

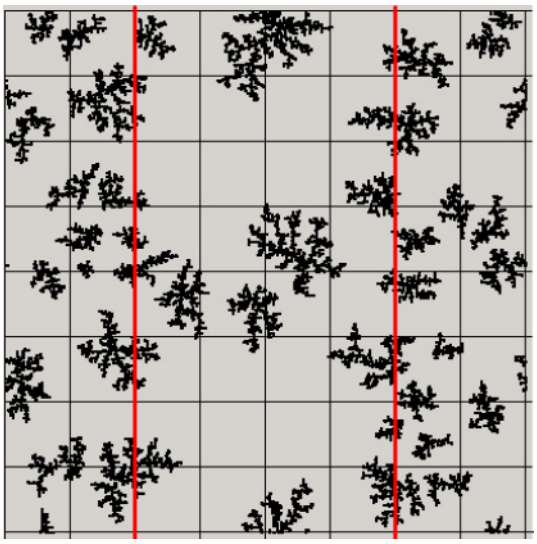

Fig. 11. (Color online) KMC simulations of Fe island nucleation on wedged Pb films at RT with different diffusion barriers in the two regions.

The underlying physics giving rise to the QSE on surface diffusion barrier might be rather complex. The experiment[66] has revealed that the highest occupied quantum well states near Fermi level show an oscillatory behavior in Pb films, which will likely affect the adatom surface binding energies. First-principles calculations[64,65] showed the Pb adtaom binding energies on the Pb(111) surface at both the minimum-energy (hcp hollow sites) and the saddle (fcc hollow sites) points oscillates with film thickness but with different oscillation magnitude, leading to an oscillating diffusion barriers. In the general, the adatom has lower binding energy and higher diffusion barrier on a more stable film than those on a less stable film.

In summary, three different experiments, homoepitaxial growth of Pb thin films, STM stimulated Pb island growth and Fe island growth, consistently reveal the interesting aspect of surface kinetic processes in this quantum system. The observed oscillating growth behavior in all three cases strongly suggests that it is a result of the electronic structure modulation by QSE along the film normal direction.

4. Band Structure Determination and Film Stability Interpretation

To understand the magic stability of the Pb films, including the unique growth behaviors discussed above, photoemission study was performed. In a photoemission experiment, the QWS of a flat thin film are characterized as a set of discrete sharp peaks in the PES spectra [Fig. 3(c)]. By fitting the energy (the peak position) of QWS in Fig. 3(c) with the phase accumulation model,[2,3] the band structure of Pb can be obtained. For s–p metals, the quantized energy levels (or QWS) are often described with the phase accumulation mode,

$$2k(E)Nd + \phi_s(E) + \phi_i(E) = 2\pi n, \qquad (1)$$

where $k(E)$ is the electron wave vector along the ΓL(111) direction, $\phi_s(E)$ and $\phi_i(E)$ are the phase shifts for an electron upon reflection at the surface and the interface, respectively. n (an integer) is the QWS index, N is the number of atomic layers in the film, and $d = 2.8435$ Å is the lattice spacing along the ΓL direction.[67]

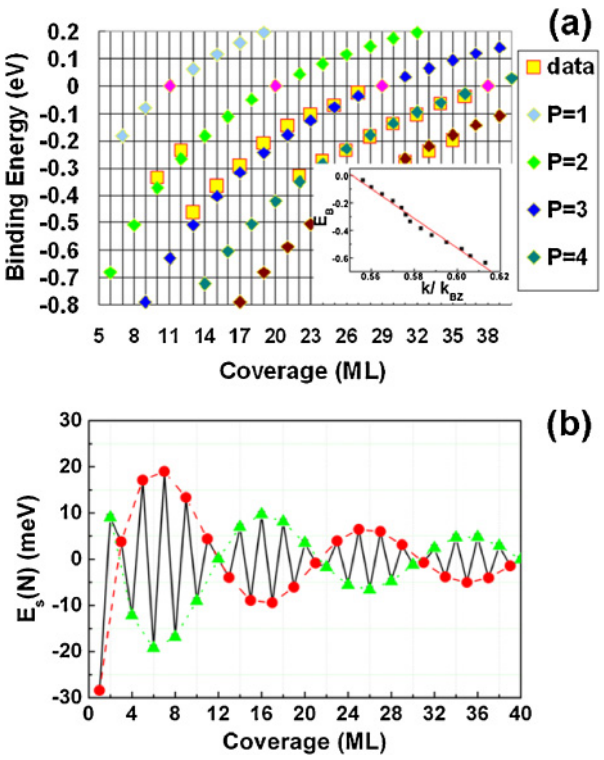

Fig. 12. (Color online) Binding energy of the QWS as a function of Pb film thickness (the shadowed squares and diamonds correspond to the experimental and the fitting results, respectively). For each measured "branch", the reduced quantum member P is indicated in the right panel of the figure. The inset shows the experimental energy band $E(k)$ along the ΓL direction in the first Brillouin zone. (b) Calculated relative surface energy as a function of Pb film thickness.

Because the phase shift depends strongly on the electron energy, the wave vector $k(E)$ at a given energy can be calculated with a simple formula,

$$k(E) = \pi(n_2 - n_1)/[(N_2 - N_1)d], \qquad (2)$$

where N_1 and N_2 correspond to the film thicknesses with the same QWS energy (E), and their index is labeled with n_1 and n_2, respectively. $k(E)$ as determined by this method is shown in the insert of Fig. 12(a), where the QWS energy exhibits an approximately linear dependence on k. Since this energy band comes from band folding from the second Brillouin zone, we fit the band using $E = -[\hbar^2(2k_{BZ} - k_F)/2m_e^*](k - k_F)$. The fitting yields an effective electron mass of $m_e^* = 1.2m_e$ (m_e is the free electron mass) and a Fermi wave vector of $k_F = 0.611$ Å^{-1}, or $k_F' = 2k_{BZ} - k_F = 1.598$ Å^{-1} before the band folding. This value is very close to the value of 1.596 Å^{-1} obtained from the de Hass–van Alphen measurement within an extended Brillouin zone scheme.[67,68]

We further fit the QWS energy in the E–d plane [Fig. 12(a)] by assuming a linear dependence of the total phase shift on energy, i.e., $\phi_s + \phi_i = \pi(a \times E + b)$. The fitted result (diamonds) is in good agreement with the experimental results (shadowed squares). The value of $k_F = 0.611$ Å^{-1} leads to a Fermi level crossing of the QWS at every $\Delta N = \pi/(k_F d)(\mathrm{ML}) = 1.8$ ML, similar to a previous theoretical calculation.[57] This explains our photo-

emission data in Fig. 3(c) that the highest occupied QWS above 21 ML oscillates (with respect to E_F) with a nearly 2 ML period. The 2 ML oscillation was found to result in a spectacular oscillation of the superconducting transition temperature, as discussed below.[36,37]

The small difference between $2k_F$ and k_{BZ} generates a "beating effect" with an oscillation period of $\pi/(2k_F - k_{BZ}) = 9$ ML,[57] since the thickness of a film is always an integer in terms of the number of atomic layers. In Fig. 12(a), the QWS labeled with index P (defined as $P \equiv 3N - 2n$) crosses E_F with a 9 ML period. Whenever the QWS of an odd (even) branch P crosses E_F, there will be a switching of the film stability from odd (even) to even (odd) layers. This even–odd switching occurs at 13, 22, and 31 ML, respectively, with an interval of 9 ML. In particular, the films become most unstable if their QWS is right at E_F. This situation appears at 11, 20, 29, and 38 ML, again with an interval of 9 ML.

Based on the "electronic growth" model, we can understand the novel stability of the Pb films. From our experiment, for $P = 2$ (10, 12 ML) and $P = 3$ (13, 15, 17, 19, 21 ML), the occupied QWS of the stable films has a lower energy than the adjacent unstable layers. With increasing film thickness, the energy difference between the odd and even layers becomes smaller, eventually leading to a quasi layer-by-layer growth above 21 ML. Relative surface energy calculation can provide us a global understanding of the novel stability as a function of film thickness.[69] Based on the experimental results, we calculated the surface energy of the Pb films in a Friedel form[32]

$$E_s(N) = A\frac{\cos[2k_F(N + \Delta N)d]}{(N + \Delta N)^{\alpha}} + B, \qquad (3)$$

where $k_F = 1.598\,\text{Å}^{-1}$ from our experiment, $d = 2.8435$ Å is the atomic layer spacing, $\alpha = 0.938$, and A and B are constant. ΔN is the additional thickness caused by the quantum well width change associated with the charge transfer between the Pb overlayer and the substrate. As shown in Fig. 12(b), eq. (3) represents a damped sinusoidal function with a Friedel oscillation wavelength that is half of the Fermi wavelength (1.8 ML in Pb), riding on an envelope "beating" function with a 9 ML internodes distance. The film stability observed in our experiments is consistent with this calculation.

Clearly, the stability of the Pb films is closely related to the electronic structure or the formation of QWS, thus is modulated by the QSE. The double-layer growth mode and turn-over points observed in the growth behavior discussed in §3 are simply a manifestation of this effect.

5. Novel Properties of Pb Thin Films Induced by Quantum Size Effects

5.1 Local work function

Work function, defined as the minimum energy required for an electron to escape from the surface, is one of the most fundamental properties of a material, as it determines the degree of difficulty of electron emission as well as the surface reactivity of the material. With the rapid development of lower-dimensional electronic devices, LWF measurement of nanostructures becomes more and more important in order to understand how electron behavior changes via geometric confinement in the nanoscale.[70] The theoretical and experimental studies on the LWF changes due to the alkali metal adsorption,[71] the crystallographic orientation[72] and the surface steps[73] revealed that the changes are closely related to the local density of states near the Fermi level.

As shown above, the formation of QWS dramatically modulates the DOS(E_F) when the film thickness is varied. LWF should show similar quantum behavior with respect to local thickness change. Previous studies have shown the evidence of an oscillatory work function over film thickness,[74–79] however, experiment measurement of LWF of a nanostructure is essentially difficult since it requires high spatial resolution and high sensitivity in terms of the very local variation.

In the past, several approaches such as photoemission from adsorbed xenon (PAX),[80] two-photon photoemission spectroscopy (2PPE),[81] and local Kelvin cantilever[82] have been developed to study the LWF. Nonetheless, it has been shown that STM with a lock-in technique is, to date, the most powerful tool for imaging the morphology, as well as the LWF with atomic resolution, for example, for Au/Cu(111)[83] and Pd/Cu(111).[84] As a matter of fact, Binnig and Rohrer, the inventors of STM, are the first to measure the LWF for metal and semiconductor in the very early stage of STM.[85] The LWF is closely related to the potential barrier between the STM tip and the sample surface. Hence, one can measure the LWF by changing the STM tunneling distance and then monitoring the response in the tunneling current.

For Pb films, Wei and Chou theoretically predicted that the LWF changes with the thickness.[57] To establish a convincing relationship between LWF and QSE, in this study we used wedge-shaped Pb islands grown on vicinal Si(111)7 × 7 substrates (see §3.2),[4,5] which allow continual measurement of the LWF at different thickness N under identical conditions. In the measurement, a sinusoidal ac voltage signal at 2.0 or 3.0 kHz was applied on the z-axis piezo of the scanner to modulate the distance between the tip and sample surface within a range of 0.7 Å. Response tunneling current was collected by a lock-in amplifier to yield the LWF images. The morphology and LWF images were collected simultaneously. STS measurement was carried out to characterize evolution of QWS with N by applying a modulation signal to the sample bias at the same frequency (2.0 or 3.0 kHz) with the bias ramping from −1.5 to 1.5 V to record the differential tunneling current also by lock-in.

Figure 13(a) shows an STM image of the Pb islands with thickness increasing from left (11 ML) to right (15 ML). The inset shows the atomic resolved STM image of the top (111) surface. A cross-section profile along the back line scan in Fig. 13(a) is shown in Fig. 13(b), which reveals the flat top nature of the Pb island despite that it is crosses laterally several Si steps.

Figures 13(c) and 13(d) show the topography and LWF images of the island taken simultaneously. Buried interfacial structures were observed on the topographic images, which have been explained in terms of a non-diffractive scattering of the quantized electrons in the QWS.[4,5] From the LWF image, we can see clearly the difference in terms of N: even

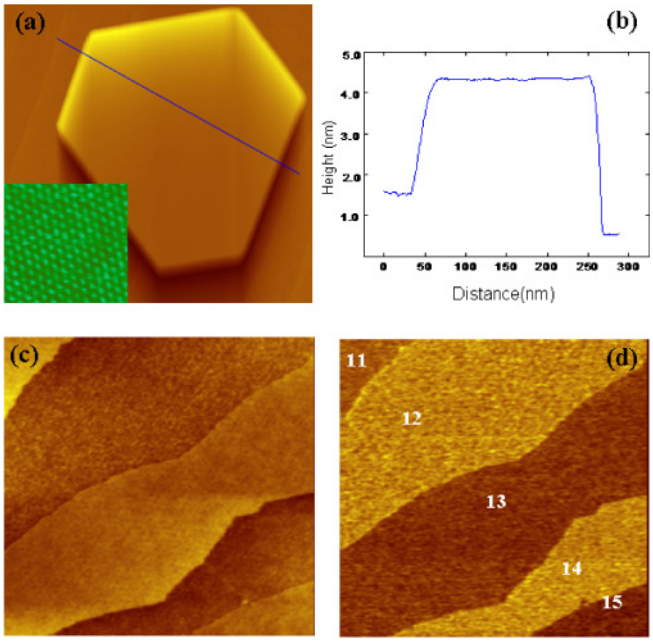

Fig. 13. (Color online) (a) STM image of a Pb island taken at $V = -0.8$ V and $I = 0.1$ nA. Image size: 500×500 nm^2. Inset is a 5×5 nm^2 atomic resolution image ($V = 0.4$ V, $I = 0.1$ nA). (b) A line plot along the indicated line in (a) to show the height profile. (c) The topographic and (d) local work function images taken simultaneously ($V = -2$ V, $I = 0.1$ nA). The bright area has a larger work function than the dark area. Image size: 337×337 nm^2.

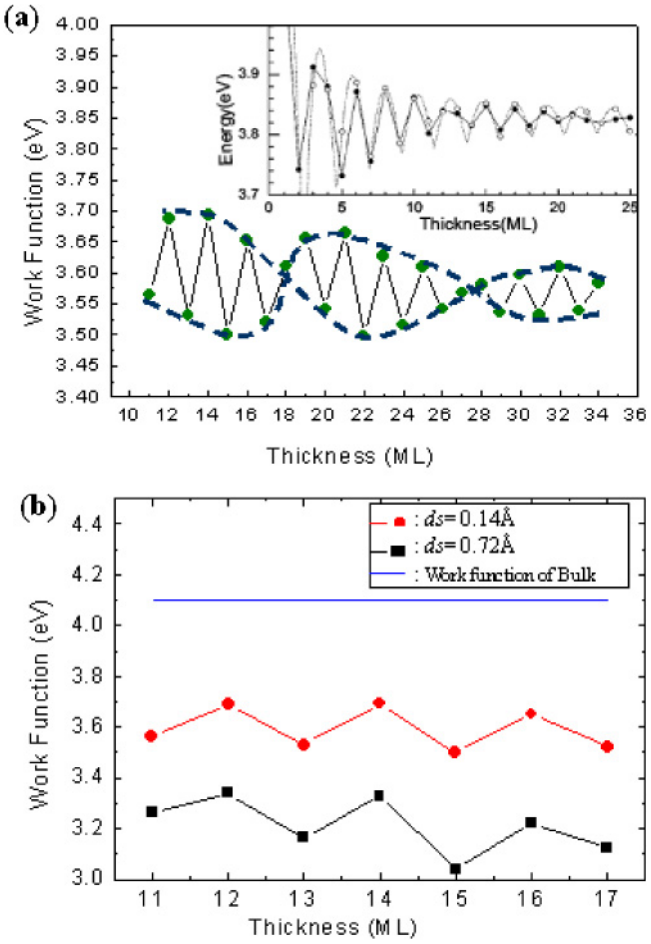

Fig. 14. (Color online) (a) The measured Pb local work function (LWF), showing a strong dependence on local film thickness N. Insert is the theoretical prediction in ref. 53. (b) A comparison of the LWF measured with modulation bias 0.1 V, modulation distance 0.72 Å and that with modulation bias 0.02 V and modulation distance 0.14 Å.

layers (12 and 14 ML) have larger work functions than odd layers (11, 13, and 15 ML). This implies that electrons in the 12 and 14 ML regions need more energy to escape from the surface than those in their respective neighboring regions.

The LWF image in Fig. 13(d) was obtained as a perturbation to the natural logarithm of the current ($\mathrm{d}\ln I$) modulated by the change of the tip–sample distance ($\mathrm{d}s$), and is strictly speaking not the LWF. According to the tunneling theory, the relationship between the current and potential barrier ϕ, which defines the LWF, can be described as $I \propto \exp(2\sqrt{2m\phi/\hbar})$. Therefore, the LWF can be written as:

$$\phi \approx 0.95\left(\frac{\mathrm{d}\ln I}{\mathrm{d}s}\right)^2. \quad (4)$$

To obtain ϕ from the LWF image, we select for each N a homogeneous and defect-free area, record $\mathrm{d}\ln I$, and then select the peak position from the Gaussian-type energy distribution on its histogram. By applying eq. (4), the value for ϕ can be obtained. Figure 14(a) shows the LWF from 11 to 34 ML, an even–odd oscillatory pattern and a 9 ML beating envelope are clearly observed. Changes in LWF reflect subtle changes in the local DOS near the E_F, as only electrons near the Fermi level can effectively contribute to the measured ϕ.

Note, however, that ϕ measured by the STS depends somewhat on the applied voltage[86] and other parameters related to the distance between tip and sample surface, so the absolute values in Fig. 14(a) may be off from the exact ones. To see this effect, we compare the results at two different modulation distances, 0.7 and 0.1 Å respectively, in Fig. 14(b). It can be understood that the deviation is larger for larger modulation distance, because in a given time $\mathrm{d}\ln I$ may not respond fully to the larger increment in $\mathrm{d}s$. However, the relative change of the LWF from layer to layer, which is the most relevant quantity in this study, does not seem to depend on the choice of either the modulation bias or the distance.

Figure 14(a) shows larger LWF for even layers than for odd layers for N between 11 and 17 ML, whereas larger LWF for odd layers for N between 19 and 26 ML. The trend reverses again at 27 ML. Overall, the bilayer oscillation of the LWF is concomitant with an envelope function of beating at approximately 9 ML. Although the oscillation in term of the exactly layer is different from the theoretical work in ref. 53 [inset in Fig. 14(a)], as free-standing film was considered in the calculation, the measured oscillatory periodicity and beating behavior show quite reasonable agreement with theory. The same trend has also been observed recently in the surface energy (see §4).[66] Such an observation can be reasonably well described by a Friedel-like function of $\lambda_F/2$ and $2d$ along the [111] direction.[15]

We resort to the DOS(E_F) revealed by the $\mathrm{d}I/\mathrm{d}V$ measurement, to explain the oscillatory behavior of the LWF. Figure 15 shows the $\mathrm{d}I/\mathrm{d}V$ spectra for $N = 13$ to 26 ML above the wetting layer. The dotted line at 0 V is the Fermi level. When N increases, the number of occupied

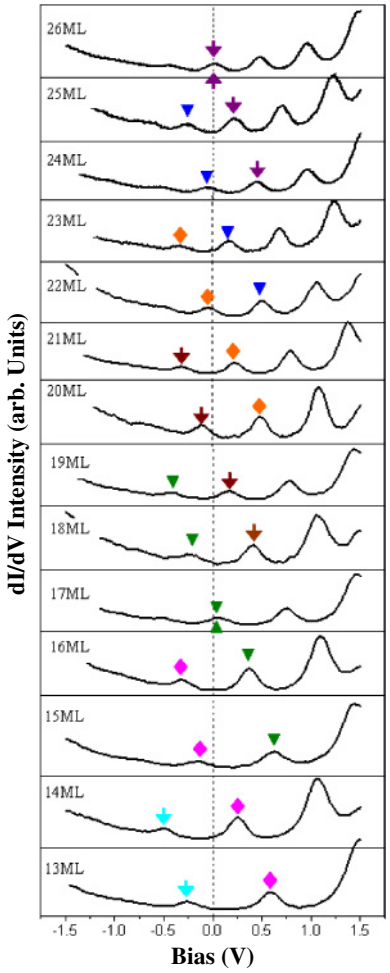

Fig. 15. (Color online) dI/dV curve of Pb films between $N = 13$ and 26 ML (without counting the wetting layer). The measurement was done at $T = 77$ K with sample bias ramp from -1.5 to 1.5 V. Same shape triangles are used here to indicate the shifts of the peak positions as a function of N, whereas upward triangles indicate the QWS peaks near the Fermi level.

quantum states also increases, accompanied by a decrease in the separation between the quantum states. According to the standing wave theory, every $\lambda_F/2$ increase in the layer thickness will introduce one more occupied QWS. So with every 2 ML increase, the lowest unoccupied QWS will move across the E_F to become occupied, as displayed by the triangles of same shape in Fig. 15. The change in the DOS(E_F), which modulates the probability of electrons for emission, causes the bilayer oscillation in the LWF. The two traversal states at 17 and 26 ML are noticeable too, as their respective peaks are very close to (but slightly above) the E_F: we note that not only 17 and 26, but also 35 and 44 ML are such critical points. They form a sequence of 9-ML interval, which coincides with the nodes in the envelope function of LWF.

One can define the energy position of the highest occupied QWS (E_{HOQWS}) with respect to the Fermi level as $\delta = E_{HOQWS} - E_F$. Figure 16 compares δ with the LWF. In terms of the oscillation pattern and beating nodes, the two quantities mirror each other perfectly, again suggesting that they are of the same physical origin. The mechanism for LWF oscillation is also manifested directly from this comparison: the higher the film density of states near the

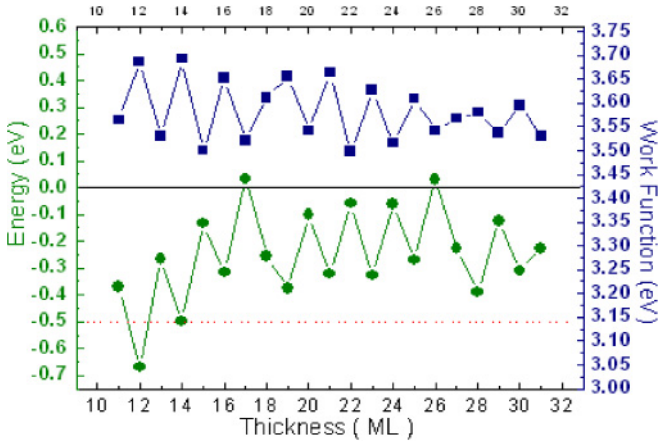

Fig. 16. (Color online) A comparison between the HOQWS and LWF. Left axis shows the energy of the HOQWS with respect to the Fermi level (= zero energy), whereas right axis shows the value of the LWF.

E_F, the lower the potential for electrons to escape, and hence the lower the work function. Within the limitation of our STM measurement, this rule is valid without exception.

The LWF study presented here reveals different work functions between even and odd layers of the same Pb(111) surface, as well as a 9 ML envelope beating pattern over a wide range of N. With the simultaneous STS measurement, we found that a smaller LWF always corresponds to a layer with its highest occupied QWS closer to the E_F. A relationship between the oscillatory LWF and the highest occupied QWS is thus established.

5.2 *Electron–phonon coupling*

Electron–phonon coupling is an important factor that determines the superconductivity of a material. For a conventional superconductor such as Pb, the effective electron–electron attraction necessary for the binding of cooper pairs is ultimately governed by electron–phonon coupling.[87] As we mentioned earlier, the formation of QWS strongly regulates the mechanical stability of films reflected with expansion and shrinkage of interlayer spacing.[88] Both of the factors speak directly to the possibility of modulating electron–phonon coupling and thus superconductivity of the Pb films.

Similar to other spectroscopy, the photoemission spectroscopy does not simply probe the ground state, rather, the resulting decayed excitations (the photoholes), and thus many-body effects such as electron–phonon coupling could be involved experimentally. Recently, prominent progress has been made in the study of the electron–phonon coupling strength (λ) for the surface states in bulk materials[89–91] or for the QWS in thin films by ARPES.[92–96] For crystalline metal surfaces, the observed photoemission peak width is proportional to $\hbar/\tau$, where τ is the lifetime of the hole state excitations. At high temperatures (greater than one-third of the Debye temperature) and small hole energies (lower than the bandwidth), the temperature-dependence of the QWS peak width is actually a good measure of the phonon contribution to the hole lifetime. Since the influence of the electron–electron interactions and the defect scattering are negligible in this case, and the inverse hole lifetime can be given by $\hbar/\tau = 2\pi\lambda k_B T$, where λ equals $2\pi k$ times the

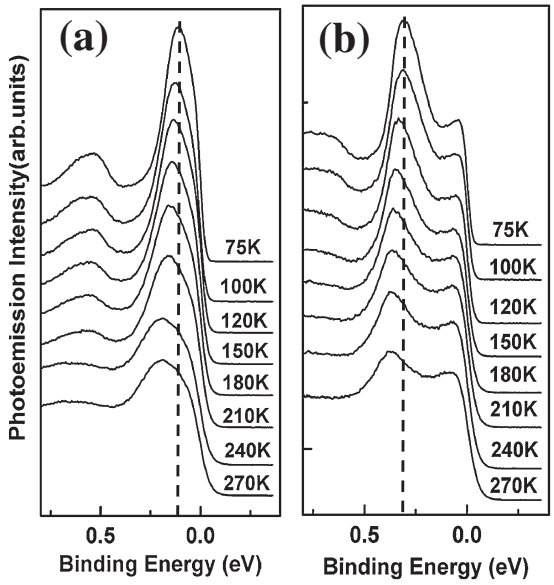

Fig. 17. Temperature-dependent photoemission spectra of Pb films for (a) 23 ML and (b) 24 ML collected within a temperature range 75–270 K. The vertical dashed lines reveal the variation of the QWS binding energy as the film temperature is changed.

slope of the peak width vs temperature. Here, we employ the temperature-dependent PES to measure λ.

The variable temperature ARPES spectra for the 23 and 24 ML films are shown in Fig. 17. With increasing substrate temperature, the peak position of the QWS shifts towards higher binding energies while the peak width broadens.[97] To find out the exact relation between the linewidth (ΔE) of the QWS and the temperature, a curve fitting by Voigt profile with Lorentzian line shape was made. The fitting results are plotted in Fig. 18(a) for the films of 22 and 23 ML, where ΔE increases linearly with increasing temperature and exhibits prominent different slopes for the adjacent layers. According to the previous discussion, this slope is related to λ via

$$\lambda = \frac{1}{2\pi k_{\mathrm{B}}} \frac{\mathrm{d}\Delta E}{\mathrm{d}T}. \tag{5}$$

The λ values derived from the QWS peaks for different film thicknesses are shown in Fig. 18(b) (triangles), where only the values for stable layers (15, 17, 19, 21, 22, 23, 24 ML) are plotted. Besides an overall gradual increase of λ towards the bulk value (1.55), an oscillation of λ with a period of 2 ML is clearly noted from 21 to 24 ML.

5.3 *Thermal expansion*

Temperature-dependence of PES spectra width was used to investigate many-body effects with regard to electron–phonon coupling.[89,94–98] Below, we would show that the peak positions, i.e., the binding energies of the QWS in the temperature-dependent spectra, could be used to understand the thermal expansion behavior of thin films. From this dependence, we could deduce the thermal expansion coefficients of the Pb films of different thicknesses along the film normal direction.

Shown in Fig. 17 are the temperature-dependent photoemission spectra of 23 ML [Fig. 17(a)] and 24 ML [Fig. 17(b)] Pb films. From the spectra, the film morphology

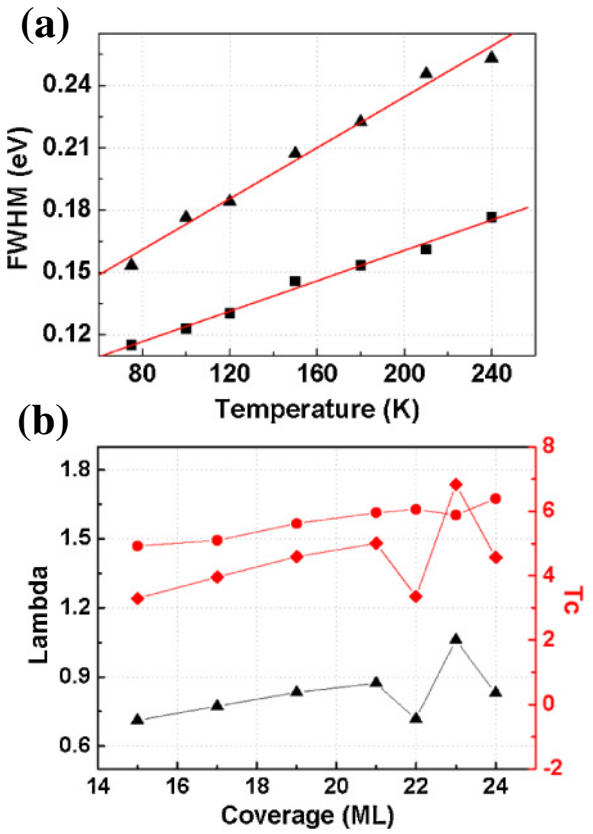

Fig. 18. (Color online) (a) Lorentzian peak widths of the QWS of the 22 ML (square) and 23 ML (triangle) films plotted as a function of temperature. (b) Measured λ (triangles) and calculated superconductivity transition temperature (diamonds) by the formula $T_{\mathrm{c}} = (\Theta_{\mathrm{D}}/1.45) \times \exp[-1.04(1+\lambda)/(\lambda - \mu^* - 0.62\lambda\mu^*)]$ as a function of thickness. In the calculation, typical values of 0.1 for μ^* (the effective Coulomb interaction) and 105 K for Θ_{D} (the Debye temperature) were used. As a comparison, the experimental transition temperature of the Pb films is also displayed (balls).

assumes an atomically flat surface over a macroscopic scale. Again, the strongest peaks correspond to the highest occupied QWS. Note that for both films including other films studied, the QWS peaks shift always towards higher binding energy with increasing substrate temperature, and the maximum shift of the QWS binding energy is less than 100 meV in a temperature range from 75 to 270 K. A dramatic difference between even and odd Pb layers can be clearly detected. For example, the net shift for the films of 23 and 24 ML are 84 and 65 meV, respectively.

Such thermal-induced binding energy shift in QWS was observed in Ag/V(100) and Ag/Fe(100) systems previously,[94,95,98] but the results were opposite: as the film temperature is elevated the binding energy increases in Ag/V(100), but it decreases in the case of Ag/Fe(100). The reason is that the substrate V(100) has a significantly lower thermal expansion coefficient compared with the Ag overlayer. For Ag/V(100) and Pb/Si(111), the behavior seems similar. Generally speaking, thermal expansion increases the lattice constants of both the epitaxial film and the substrate, which will subsequently, in terms of the simple phase accumulation model,[2,3] increase the width of quantum well and lower the Fermi level, in addition to a possible phase shift change at the interface between the film and the substrate. In a 2D

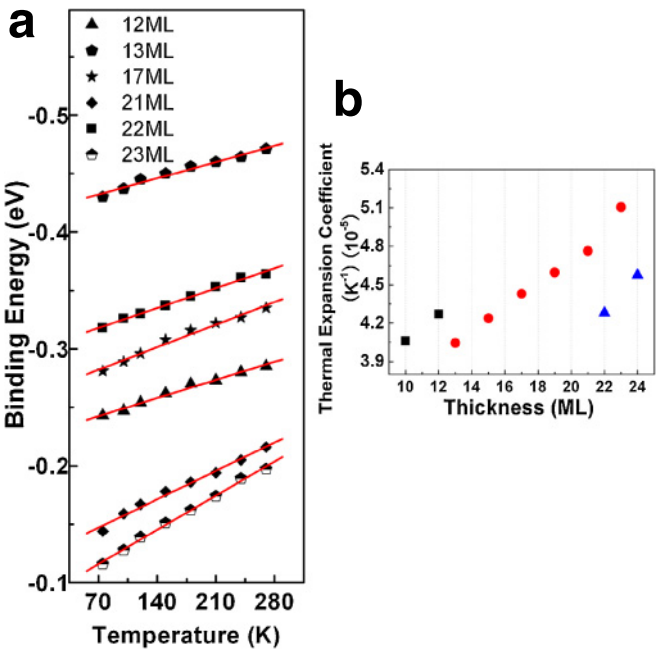

Fig. 19. (Color online) (a) Binding energy of the QWS plotted as a function of temperature. The dots and lines indicate the experimental data and linear fits, respectively. (b) Thermal expansion coefficients of the Pb films along the confined direction calculated with the proposed model.

system, change of the phase shift at the interface was proved to play minor effects.[99] Therefore, the dominant factor in the observed binding energy shift should mainly arise from the first two factors.

To quantify our results, the temperature-dependence of the QWS binding energy for several Pb films is fitted linearly and shown in Fig. 19(a). While the increased binding energy of the QWS in Ag/V(100) system was explained as that the energy of the QWS decreases more than the Fermi energy of the substrate,[94] we attribute it to a different reasons, namely the thermal broadening of the confinement well width, in addition to variation of the Fermi level of Pb films. For Pb/Si(111), when temperature (T) increases, E_F of the Pb film drops much more than E_F of Si does due to the dramatic difference in their thermal expansion coefficients, so there is a charge transfer from Si to the Pb film. These charges only stay at the Pb–Si interface (no charge is expected in Pb film), which shift up all energy levels equally of the Pb film until $E_F(\mathrm{Pb}) = E_F(\mathrm{Si})$ is satisfied. Therefore, the Fermi energy of Si and its change have minor effect on the relative shift of the QWS in the Pb film. Within a simple free electron approximation, the temperature-dependence of the Fermi energy of a bulk material is described as,

$$\mathrm{d}E_F/\mathrm{d}T = -2E_F\alpha_r, \tag{6}$$

where α_r is the linear thermal expansion coefficient of the material, and E_F is its Fermi energy relative to the bottom of valence band. For the thermal induced shift of of the substrate Fermi level, α_r can be selected as $2.8 \times 10^{-6}\,\mathrm{K}^{-1}$ (the bulk value). As for the thermal induced shift of the QWS energy, such approximation should be reasonable regarding to the fact that the QWS energies of the Pb films involved are within a small energy window of 0.6 eV below the Fermi level, which has been successfully used to determine the Pb band structure.[66] The thermal-induced shift of the QWS energy (E_{QW}) with respect to the bottom of valence band has a form of,

$$\mathrm{d}E_{QW}/\mathrm{d}T = -2E_{QW}\alpha_Z, \tag{7}$$

where α_Z is the linear expansion coefficient along the confined direction.

We calculated the linear thermal expansion coefficient of the Pb films in the confined direction by the experimental thermal shift of QWS binding energy in terms of eqs. (6) and (7), and the results are shown in Fig. 19(b). Several observations can be made: (1) the thermal expansion coefficients in the film normal direction are greatly enhanced compared to the bulk Pb; (2) there is a 2 ML oscillation for the Pb films from 21 to 24 ML; (3) the overall trend is that a lower expansion coefficient corresponds to a film with a higher QWS binding energy.

Since the thickness of the Pb films is very small, the linear expansion coefficient in the film plane (xy plane) should be very closed to that of bulk Si, while in z direction, a great enhancement can be expected because of what called Poisson effects and that the linear expansion coefficient of Si ($2.8 \times 10^{-6}\,\mathrm{K}^{-1}$) is one order of magnitude lower than that of Pb ($2.89 \times 10^{-5}\,\mathrm{K}^{-1}$). To understand the global enhancement of the linear thermal expansion coefficient along the confined direction, we use α_r, α_P, and α_Z to describe the linear expansion coefficient of the free standing film, the confined film in the film plane, and the film normal (z) direction, respectively. α_Z can be expressed as

$$\alpha_Z = \alpha_r + \frac{2(\alpha_r - \alpha_P)\eta}{1-\eta}, \tag{8}$$

where η is the Poisson ratio. Substituting α_r and α_P by the linear expansion coefficients of bulk Pb and bulk Si, respectively, and taking η as the Poisson ratio of bulk Pb (0.44), we obtain that α_Z equals $2.414\alpha_r$. That means, in an ideal case, the thermal expansion in z direction should be enhanced by 2.414 times of the bulk value, which is adequate to explain the global enhancement of our experimental data in Pb/Si(111).

Another important feature is the periodic oscillation of the thermal expansion coefficient. Note that λ_F of Pb is nearly four times of the atomic plane spacing (d_0) along the (111) crystallographic direction, namely $\lambda_F \approx 4d_0$, thus, the periodicity for the Fermi level crossing of the QWS is about 2 ML. This has been used to account for the bi-layer oscillation in Pb film stability.[57] A straightforward explanation of this oscillatory phenomenon comes from the so-called misfit function,[100,101]

$$\delta(n) = \left| nd_0 - m\frac{\lambda_F}{2} \right|, \tag{9}$$

where n is the number of atomic layers, and m is an integer and will be selected to make δ a minimum. Generally speaking, a dramatic mismatch, a large δ, will not make the electron standing wave fit properly into the potential well (nd_0). For the Pb films of 21 or 23 ML with a lower QWS binding energy, δ is close to $\lambda_F/4$ (its maximum value). In this case, further change (either decrease or increase) of the confinement well width will always decrease the mismatch

and thus the system energy, making the expansion easier. Consequently, a large expansion coefficient can be expected for an unstable film with a large δ. On the other hand, for a stable layer (22 or 24 ML) with a higher binding energy and a small δ (close to 0), expansion will always increase the mismatch between nd_0 and $m\lambda_F/2$, is more energetically unfavorable. Hence, the oscillatory film stability and expansion coefficient are of the same origin, and are due to the electronic energy quantization[41] in this system.

5.4 *Superconductivity*

2D thin film superconductors are defined by reducing the material size below the coherence length in one direction.[102] For conventional superconductors such as Pb, the coherence length ξ_0 (83 nm for Pb)[103] is very large compared to atomic dimensions and the electron Fermi wavelength (λ_F) ($\sim$1.06 nm). Therefore, 2D superconductors are still made of 3D electrons; only the condensate wave function for the cooper pairs may be regarded as 2D. A common trend of such 2D superconductors is that the transition temperature T_c is reduced continuously as the film thickness is decreased, which is caused by enhanced quantum fluctuations of the phase of the condensate wave function for thinner films.[104,105] Oscillatory behavior in T_c from QSE was suggested in early theoretical works,[106,107] and experimental observation of such effect was claimed in an experimental study of thin Sn films.[12] However, the observed T_c oscillations differed quantitatively from the theoretical predictions and there was no corresponding oscillations in the normal state resistivity as expected. The results were explained later[108,109] as due to QSE in the grain structures of the films which were indeed typically polycrystalline and granular in nature. Conductance measurement of ultrathin Pb films on Si(111) showed clear variations in T_c, but the data was insufficient to establish an oscillating period.[110]

As shown above, we are able to grow ultra-thin crystalline Pb films on Si(111) substrate with atomic-scale uniformity in thickness over a macroscopic area, and thus can make transport measurement on the film and identify the superconducting transition temperature as a function of the number of atomic layers in a well-controlled manner.

The thickness-dependent photoemission spectra measured *in situ* from these samples [Fig. 3(c)] show well-defined QWS peaks, which shift progressively in energy as the film thickness is increased by each atomic layer. Because of the progressing of the QWS in energy as a function of film thickness and their discrete nature, the position of the highest occupied QWS oscillates with respect to E_F (0.0 eV) between the odd and even layers. This is further confirmed by our first-principles calculations which show the same oscillatory behavior with higher density of states near E_F for the odd layers and lower ones for the even layers. As most physical properties, such as superconductivity, depend strongly on the distribution of electrons near E_F, we expect that these properties would also be modulated as a function of film thickness accordingly.

Figure 20 shows the superconducting transition temperature T_c (black solid balls) as a function of film thickness. Here, T_c is defined as the temperature at which the film resistance becomes half of the normal state resistance at $T = 8$ K, as indicated by the arrow in the inset of Fig. 20.

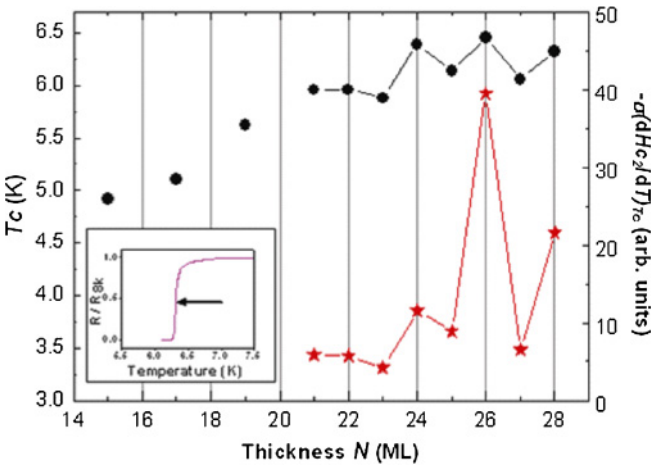

Fig. 20. (Color online) Superconducting transition temperature T_c (black solid dots) and density of states $N(E_F) \propto -\sigma(dH_{c2}/dT)_{T_c}$ (stars) plotted as a function of Pb film thickness, clearly demonstrating an non-monotonic oscillatory behavior in both T_c and $N(E_F)$. The insert shows the resistance as a function of temperature measured from the 28 ML film, which reveals a sharp transition to superconductivity at 6.32 K, as indicated by the arrow.

We can clearly see that there is an overall trend of increasing T_c with increasing film thickness, which is consistent with the behavior of conventional 2D superconductors. Most strikingly, there is an oscillatory behavior in T_c above 21 ML with an oscillating period of 2 ML: a higher T_c for the even number thickness and lower T_c for the odd number thickness. Monotonic behavior below 21 ML is observed, but there the intervening even layers are missing.

According to the Bardeen–Cooper–Schrieffer (BCS) theory of superconductivity, T_c depends exponentially on the electron density of states at the Fermi energy $N(E_F)$ and phonon-mediated attractive interaction V between the electrons in the form of

$$T_c = 1.14T_D \exp[-1/N(E_F)V], \tag{10}$$

where T_D is the Debye temperature characterizing the energies of the phonons. From the above discussion, we know that the presence of QWS can strongly modulate the $N(E_F)$, and thus the oscillatory T_c should be closely related to the formation of QWS in the films. For a system in which the QSE are involved, $N(E_F)$ oscillates as $N(E_F) = (m^*/\pi\hbar^2 t)[2t/\lambda_F]$ as a function of the film thickness t, where m^* is the effective mass of electrons, $\hbar$ is the Planck constant, and $[2t/\lambda_F]$ is the integer part of $2t/\lambda_F$. In our case, the Fermi wavelength λ_F of Pb is about 4 ML, which corresponds to an oscillating period of 2 ML.[15] When the film thickness fits to the integer times of half wavelength, resonance of QWS occurs.

To further identify the role of the QWS modulated DOS in the transition temperature, we also performed magnetoresistance measurement to estimate more accurately the DOS near the superconducting state. The photoemission data we showed before cannot be directly used for this purpose for two reasons. First, those data were collected along the normal-emission direction (perpendicular to the sample surface), which is an incomplete measurement of the DOS. Second, those data were obtained *in situ* on the bare Pb films

without the Au coverage (while the T_c were obtained with an Au cap cover); preliminary theoretical and experimental studies show that the Au coverage can significantly shift the energy positions of the QWS in the Pb films because of the change of boundary conditions. According to the Ginzburg–Landau–Abricosov–Gorkov theory, $N(E_F)$ of a Pb film is proportional to the slope of the perpendicular upper critical field $H_{c2\perp}$ in its temperature dependence near T_c,

$$N(E_F) \propto -\sigma(dH_{c2\perp}/dT)_{T_c}, \tag{11}$$

where σ is the normal state conductivity. We measured the film resistance (R) as a function of applied magnetic field (H) along the surface normal direction at different temperatures. To avoid trapping flux in, the magnet was discharged to zero in oscillating mode and the sample was warmed up to 8 K before R–H measurement for each temperature. Then the perpendicular upper critical fields $H_{c2\perp}$ at different temperatures were obtained from the R–H measurements at the field where the resistance reached half of the normal state resistivity R_N. The resistance approaches R_N very gradually because of the magnetoresistance effects. So we take R_N as the resistance where the resistance variation ratio is within 0.1%. In order to remove the influence from the Au cap layer, the normal state conductivity of the Pb films is estimated from the inflexion point of the R–T curves. The measured value (stars) of $-\sigma(dH_{c2\perp}/dT)_{T_c}$, which is proportional to the density of states $N(E_F)$, is plotted in Fig. 20, a one-to-one correspondence between $N(E_F)$ and T_c in their thickness dependence is clearly observed.[111]

Of course, electron DOS is not the only factor affecting the superconductivity transition temperature. For a conventional superconductor such as Pb, electron–electron attraction necessary for the binding of cooper pairs is ultimately due to electron–phonon interactions.[87] As we mentioned earlier, QWS strongly regulates the mechanical stability of films at different thicknesses, and it is also known that they can cause expansion and shrinkage of interlayer spacings.[88] Both of these facts speak directly to the possibility of modulating electron–phonon coupling by the QSE. In §5.2, we deduced electron–phonon coupling coefficient λ from the temperature dependence of the widths of QWS peaks, and observed the oscillation of λ above 21 ML. As a comparison, the measured λ, T_c for the Pb films and the calculated T_c from formula $T_c = (\Theta_D/1.45)\exp[-1.04(1+\lambda)/(\lambda - \mu^* - 0.62\lambda\mu^*)]$ are shown in Fig. 18(b). A clear correspondence between λ and the experimental T_c for different layers is obvious, but the variation trend is inversed in amplitude vs thickness above 21 ML. That is to say, a larger λ corresponds to a lower T_c, which can also be explained by the affection of the Au protection layer for T_c measurements.

The perpendicular upper critical field $H_{c2\perp}$, is an important physical parameter for superconductivity. We also investigated the dependence of the upper critical field on film thickness. The R–H measurements and the method to obtain $H_{c2\perp}$ have been described above.

Figure 21 shows the R–H curves of a 21 ML sample at different temperatures. The arrow points out the defined perpendicular upper critical field at 4.7 K. The upper critical field $H_{c2\perp}$ as a function of temperature is shown in the inset of Fig. 21. We observe a perfect linear dependence on T near T_c, which is typical for a superconductor with a high

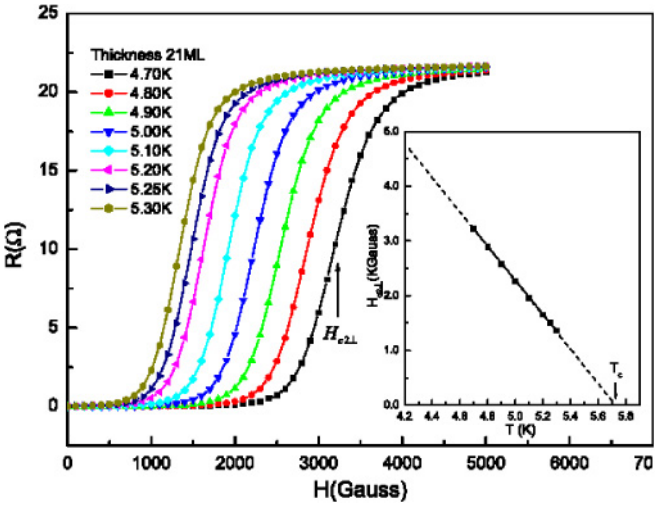

Fig. 21. (Color online) R–H curve of the 21 ML sample. The magnetic field is perpendicular to the sample surface. The black arrow indicates the determined upper critical field at 4.7 K. The inset shows the $H_{c2\perp}$ as a function of T for this sample. The plot is linearly extrapolated with dashed lines to both high and low temperature sides. The measurements were carried out with a quantum design magnetic property measurement system (MPMS-5).

value of the Ginzburg–Landau parameter κ. The inset of Fig. 21 can be used to determine the zero field critical temperature T_c by extrapolating the plot to $H_{c2\perp} = 0$. T_c as a function of thickness, determined in this way, is shown in Fig. 24(a). Normally, a direct way of determining critical temperature is through the R–T measurement at zero fields. We find that the critical temperatures determined by both methods shows a consistent oscillation behavior and the values are quite close for every thickness.

The reduced R–T curves of Pb films from 21 to 28 ML are shown in Fig. 22(a). The normal state resistivity ρ_n oscillation with film thickness at $T = 8$ K is shown in Fig. 22(b). Oscillating behavior either in normal state resistivity[112,113] or in T_c[12] caused by the QSE was reported in single crystalline films or in polycrystalline films, respectively. In our experiments, the distinct oscillation with a defined period of 2 ML of both T_c and ρ_n were observed, which indicates that the QSE shows up in both the superconducting state and the normal state, suggesting the high quality of our films. However, the intensities and mechanism may vary in different ways depending on the sample conditions.

Figure 23(a) shows $H_{c2\perp}$ as a function of reduced temperature $t = T/T_c$. For every thickness, the $H_{c2\perp}$ shows a good linear dependence on t at $t = 1$. $H_{c2\perp}$ vs film thickness for $t = 0.90$ and 0.95 are shown in Fig. 23(b). It reveals that with the film thickness variation $H_{c2\perp}$ exhibits an oscillation behavior that is similar to the reported T_c oscillation.[36,37] However, the oscillation of $H_{c2\perp}$ are π out of phase to that of T_c, i.e., peaks appears in the odd layer samples where dips appear in the even layer samples, which is opposite to the T_c oscillation shown in Fig. 24(a).

In the early theories on the magnetic properties in thin film superconductors, the Tinkham–de Gennes–Saint-James (TGS) theory[114,115] was valid showing a good agreement with the experimental results.[116,119] According to the

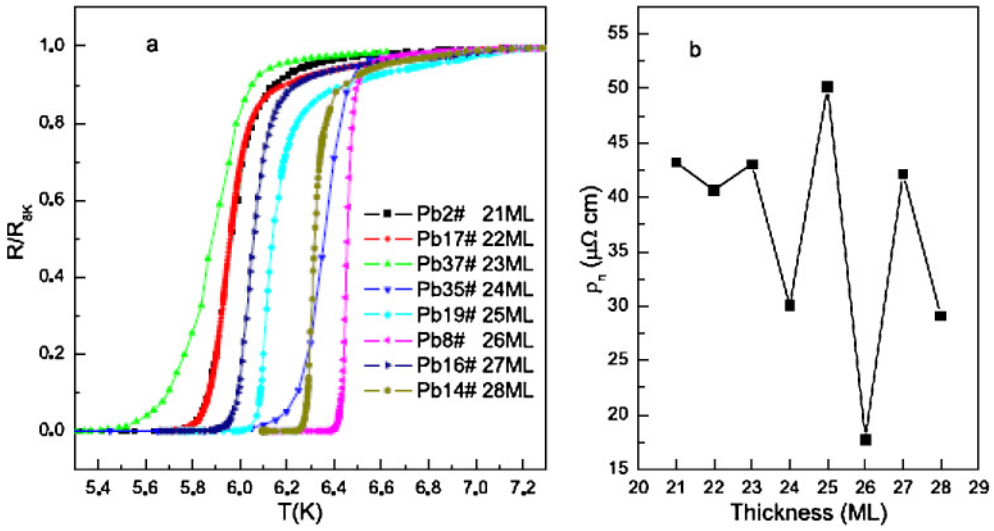

Fig. 22. (Color online) The reduced resistances of Pb films as a function of temperature are shown in panel (a). The resistances are normalized by the normal state resistance at $T = 8\,\mathrm{K}$. Panel (b) shows an oscillation of normal state resistivity at 8 K as a function of film thickness.

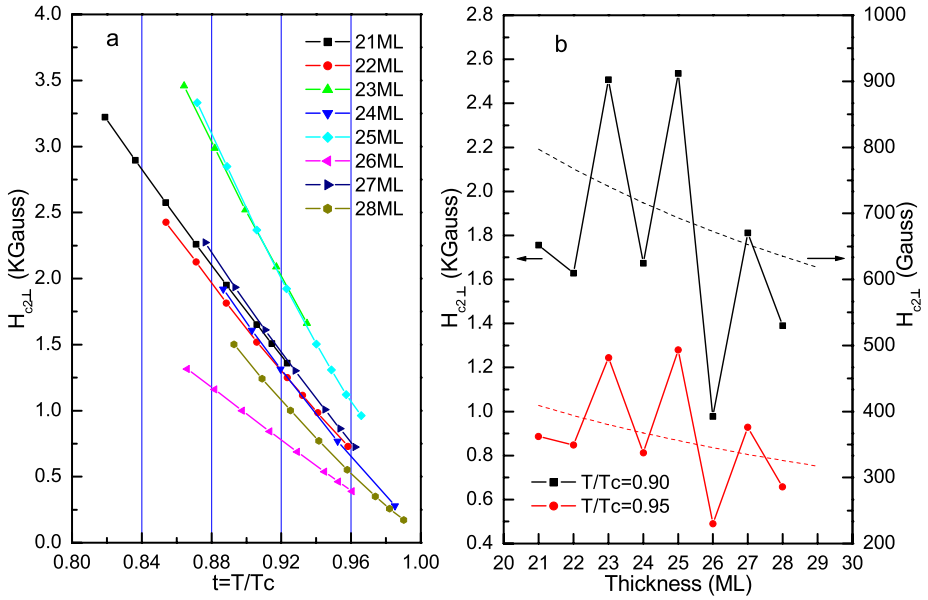

Fig. 23. (Color online) Panel (a) shows the perpendicular upper critical field vs the reduced temperature t. the oscillation behavior at $t = 0.9$ and 0.95 are plotted in panel (b). The dashed lines correspond to the calculated results using eq. (12).

TGS theory, the upper critical fields $H_{c2\perp}$ near T_c should monotonically increase with decreasing film thickness, which can be described as

$$H_{c\perp}(T,d) = \sqrt{2}\kappa(T,\infty)H_c(T)(1 + b/d), \qquad (12)$$

where $\kappa(T,\infty) = 2\sqrt{2}\pi H_c(T)\lambda_\infty^2(T)/\phi_0$ and $b = 3\lambda_L^2(T)\xi_0/8\lambda_\infty^2(T)$. Here $H_c(T)$ is the thermodynamic critical field, λ_L is the London penetration depth λ_∞ is the bulk weak field penetration depth, ϕ_0 is the flux quantum ($\phi_0 = hc/2e = 2.07 \times 10^{-15}\,\mathrm{Wb}$), and d is the film thickness. The dashed lines in Fig. 23(b), calculated using eq. (12) and the related parameters in previous work[116–118] with film thickness appropriate to our samples, shows the same tendency as the experimental curves if the oscillation are ignored. The measured $H_{c2\perp}$ values of our sample are three times larger than the calculated values (note the different scales on the two sides of Fig. 23(b), which may be caused by stronger interface or impurity scattering in our films that gives rise to a large resistivity, thus large $H_{c2\perp}$ (see discussion below). The linear dependence on t shown in Fig. 23(a) also gives information that for a given film thickness, the temperature dependence follows reasonably well with eq. (12) whether that particular film is at the peak or valley of the $H_{c2\perp}$ oscillation.

The TGS theory above includes surface scattering effects but does not consider the QSE that occurs in thin films. The absent $H_{c2\perp}$ oscillation from the TGS theory means that the thickness dependent QSE is the origin of the $H_{c2\perp}$ oscillations. According to the Ginzburg–Landau (GL) theory, $H_{c2\perp}$ is determined by the in-plane coherence length $\xi_{//}$. In a 3D anisotropic superconductor, the perpendicular upper critical field near T_c is given by $H_{c2\perp} = \phi_0/(2\pi\xi_{//}^2)$. Our ultrathin films are thinner than 10 nm, which is much smaller than the Pipard coherence length of

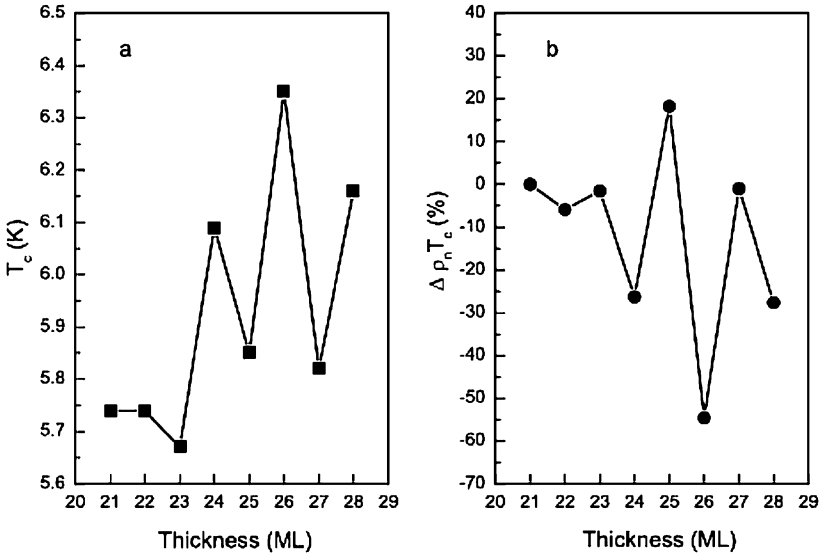

Fig. 24. Panel (a) shows the oscillation behavior of T_c with film thickness, which is defined by the way shown in the inset of Fig. 20. The rescaled $\rho_n T_c$ variation is shown in panel (b), which is defined in the following way: $\Delta\rho_n T_c = (\rho_n T_c - \rho_n' T_c')/\rho_n' T_c'$, where $\rho_n' T_c'$ is the value of $\rho_n T_c$ for the 21 ML film.

bulk superconductor ($\xi_0^{\text{bulk}} = 83$ nm). Using the quasi-2D formula[120]

$$\left(\frac{dH_{c2\perp}}{d(T/T_c)}\right)_{T_c} = -\frac{\phi_0}{2\pi\xi_{//}^2}, \tag{13}$$

for the linear dependence on t near $t = 1$ shown in Fig. 23(a), $H_{c2\perp}$ has the same oscillation behavior with the thickness as that of $-(dH_{c2\perp}/dt)$ at a certain t. The system should be considered as a dirty-limit superconductor because of the strong scattering. For dirty superconductors near T_c, $\xi_{//}^2 \approx \xi_0 l$, where ξ_0 is the Pipard coherence length and l is the mean free path for a film.[121,122] According to the BCS theory, $\xi_0 \propto 1/T_c$; therefore we can get $H_{c2\perp} \propto T_c/l$ at a certain t. In Fig. 23(b) and Fig. 24(a), it is shown that the oscillation amplitude of $H_{c2\perp}$ and T_c are about 40 and 10%, respectively. On the other hand, the mean free path l and the normal state resistivity ρ_n have the following relation: $l = 1/\rho_n$, from which we can derive $H_{c2\perp} \propto \rho_n T_c$. In Fig. 22(b), the ρ_n oscillation shows an amplitude of about 60% larger and the same phase as $H_{c2\perp}$. The rescaled variation of $\rho_n T_c$ is shown as $\Delta\rho_n T_c$ in Fig. 24(b), which fits well with the oscillation behavior of $H_{c2\perp}$. It implies that the ρ_n oscillation dominates over the T_c oscillation in $H_{c2\perp}$ and gives rise to a π phase shift between T_c and $H_{c2\perp}$ oscillations. In earlier works, effects of impurity and surface/interlayer roughness on QSE in thin films were theoretically discussed.[123–125] Although at the moment, we do not have a complete answer to the oscillation behavior of ρ_n with thickness for our films, the previous experiments on the layer spacing oscillation provide a strong indication that the modulation of the interface roughness with thickness may play an important role. In that experiment, the interlayer spacing was found to oscillate with a period of quasi-double-layer and even-monolayer samples have shorter interlayer spacing. This is also supported by the QWS binding energy modulation observed above.[36,43,66] The unaccommodating lattice and conduction electrons in the odd-layer samples could induce some lattice distortion and therefore enhance the interface roughness. This enhanced interface roughness might induce a higher resistivity.

We believe the experimental findings in our ultrathin films are due to a variety of QSE. The QSE can show up as either a modulation of the interface roughness induced by the interlayer spacing or a modulation of the phonon modes and the electron phonon coupling, both of which affect the normal state transport properties of the samples, of course, also causing the wave vector quantization along the thickness direction. Under the circumstance, only the components of the electronic wave vector in surface plane, i.e., the x–y plane, have a continuous distribution. Therefore, the electron density distribution is rather inhomogeneous along the z direction. The modulation of the electron density may further feedback to the electron-interface and the electron–phonon scattering process and therefore to the mean free path. Another relevant issue is that the GL theory is only a mean field theory, in which all the short distance fluctuations are integrated out. For our ultrathin films, to give an adequate description of all the electronic states and the scattering process, we must go back to the microscopic theory of BCS superconductivity within the subband framework and derive the multiband GL theory. The GL order parameter ψ perpendicular to the film is limited to quantized values and may also show modulation with the interlayer-spacing modulation. Each subband may have a different value of coherence ξ in the x–y plane, namely, $\xi_{n,d}$, where n is the subband index and d is the number of monolayer. In general, $H_{c2\perp}$ is determined by a matrix equation with m being the size if the matrix in which m is the number of subband below the Fermi energy. In the limit that one of the $\xi_{n,d}$ is much smaller than others, $H_{c2\perp}$ is predominately determined by this minimum value, which could be much higher than that of the bulk. The story here is similar to that of the newly discovered superconductor MgB_2, where only two bands are involved.[127,128] If the film becomes thicker, the number of subbands will increase. The interaction of subbands will weaken the QSE and the coherence length will be close to the average one. The oscillation of $H_{c2\perp}$ eventually disappears beyond a certain thickness.

The $H_{c2\perp}$ oscillation observed is opposite to that of the T_c in phase and cannot simply be attributed to the modulation of the density of states and T_c. To explain both the anomalous oscillation of $H_{c2\perp}$ and its large value, we proposed a model by considering the interface and the surface scattering and the modulation of coherence length

and mean free path induced by the QSE A qualitative description for our findings in our experiments must be based on the interlayer structures, electronic structures, phonons, and electron–phonon and electron-interface scattering processes. Further consideration about flux dynamics is also necessary by including the interface and surface scattering effects and 2D fluctuations in the multiband GL theory.

Recently, the superconductivity modified by QSE of Pb films has attracted more interesting.[129–131] The T_c oscillation was confirmed by the layer-dependent superconducting energy gap measurement by STS with a low temperature STM. Persistent quantum oscillations were observed in the energy gap and the superconducting transition temperature determined from the energy gap.[129] Using the contactless magnetic techniques, a superconducting quantum interference device (SQUID) magnetometer, the dc magnetization loops were measured for different thickness Pb films. It is found that the underdosed films with voids have the highly irreversible magnetization, implies a near-perfect bean-like critical state (a very hard superconductor) with exceptionally strong vortex pinning. While quickly depressed the magnetization is observed for overdosed films with mesas, indicating that vortex pinning with mesas is weak.[130,131]

5.5 *Adhesion force*

The adhesion is of fundamental importance for many surface and interface phenomena such as friction, wear, welding and metallic lubrication, which takes place through strong adhesive bonding formation along the interface, including ionic, covalent, metallic, hydrogen, and/or van der Waals bonds whenever two clean solid surfaces are brought into contact.[132,133] The electronic property at the surface is expected to impact a remarkable influence on adhesive behavior. As the size of objects reduced to nanoscale, the contribution from the deformation produced under light contact force becomes so small that it could be neglected, the adhesion will play a more critical role in friction, wear, welding and metallic lubrication.[134,135]

Buckley *et al.*[134,135] showed that, when contacting iron (011) plane with the surfaces of other metals, the measured adhesive forces were closely related to the chemical activity of these metals, and that the electronic structure of the metal surfaces plays an important role. Relationship between the electron work function (EWF) and its mechanical properties for 3d transition metals was also studied,[134–138] which revealed that a metal with higher EWF had a lower adhesion and friction. This was interpreted to be due to the difference in electronic behavior of these metals. In addition, chemical modification at the surface[139,140] and superconducting transition[141] were also shown to lead to significant variation in the mechanical properties of a material.

While it is generally believed that the adhesion and other mechanical properties are greatly affected by the object's electronic configuration, the change in electron properties always accompanies with other changes, for example, in chemical composition and structure at the surface in the existing studies. Atomic force microscopy (AFM) is a powerful tool for the study of adhesion in nanometer scale, however, the state of tip can vary significantly in different experiments, which makes identification of pure electronic effect on adhesion difficult.[142]

Here we employed the nanoscale flat-top Pb island on stepped Si(111) surface[4,5] to investigate the effect of electronic structure on adhesion behavior, as we did in surface diffusion study described in §3.3. Electron interference fringes were observed on the Pb wedge islands with STM, indicating a strong modification of the electronic structure by QSE when the surface structure and composition essentially remains unchanged.

We used the Omicron commercial variable temperature beam-deflection AFM sharing the same scanner with the STM as mentioned above.[143] The adhesive force was calculated from the force–distance curve,[132] and the force–distance curve was measured with contact mode, on which a soft silicon nitride cantilever with a nominal spring constant of 0.05 N/m was loaded. The cantilever was 300 μm long, 35 μm wide and 1.0 μm thick with a resonance of approximately 14 kHz. The tip apex radius was less than 10 nm. At each thickness of Pb films, which was calculated from the wetting layer to the top of the islands corresponding to specific Si(111) steps, the force–distance curves were collected at 10 different points under a temperature of 60 K. Then the adhesive forces were figured out and averaged.

The detail of the Pb islands was also described in §5.1 (Fig. 13). In Fig. 25(a), we show an AFM image of a similar Pb island prepared by the same way. The thickness of the Pb island changes by one atomic layer on every successive Si terrace, thus eight thicknesses are presented in the island.

Figure 25(b) shows the schematic force–distance curve during the contact process between silicon nitride tip and the surface of Pb(111) islands. The horizontal axis represents the tip–sample distance. The produced force at different distances is given in the vertical axis. As the tip approaches to the sample surface, at point A an attractive force comes out and pulls the tip towards the sample. The first contact between the tip and the surface occurs at point B. From this point on, when the tip is further extended, the force imposed on the tip gets stronger as indicated in the slope part of the curve. The tip experiences an adhesive regime when retracting from the surface. At point C, the tip is finally free of interaction with the surface. The horizontal distance between point B and point C multiplied by the spring constant of the cantilever gives the adhesive force.[144]

The dependence of adhesive force on thickness (from 10 to 14 ML) is presented in Fig. 26. The adhesive forces exhibit a clear oscillation behavior.

Considering[142,145] the contact between a sphere and flat surface, according to the Johnson–Kendall–Roberts (JKR) theory, the adhesive force depends on the work of adhesion w directly by

$$F = -\frac{3}{2}\pi R w, \tag{14}$$

where R is the radius of the tip. The work of adhesion w is linked to the surface energies of the Pb islands γ_1 and the tip γ_2 and their interfacial energy γ_{12} as

$$w = \gamma_1 + \gamma_2 - \gamma_{12}. \tag{15}$$

In our experiment, the tip condition is unchanged during taking the same image and the surface energy of tip γ_2

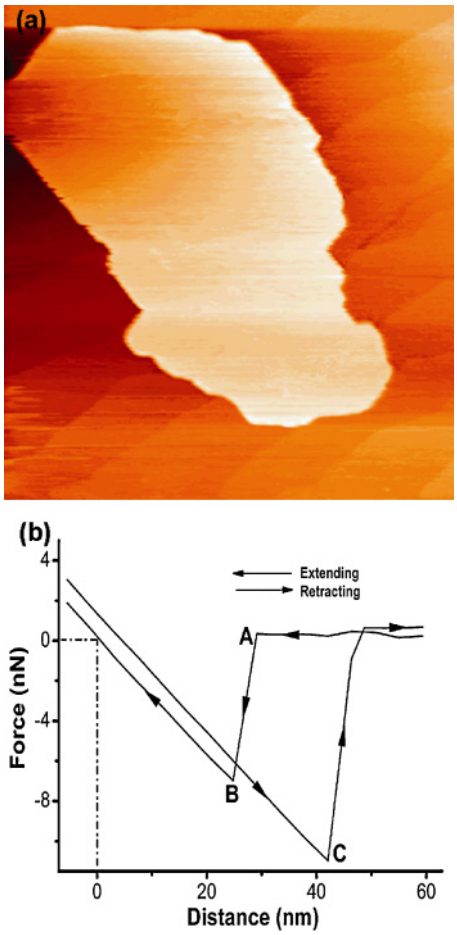

Fig. 25. (Color online) (a) A $1000 \times 1000\,\mathrm{nm}^2$ contact AFM image of a Pb island grown on a stepped Si(111) substrate, collected with the normal force of 0.2 nN. (b) The obtained typical force–distance curve for the contact between Si_3N_4 tip and the surface of Pb(111) island. The horizontal axis represents the vertical position of the piezoelectronic tube, while the vertical one is the induced force between the tip and the sample surface.

can be treated as a constant. Thus the change in adhesive force shown in Fig. 26 is owing solely to the change in surface energy at different thickness.

Surface energy is mostly determined by the surface electronic structure.[137,138,146] A semi-empirical linear equation between them is built up and expressed as:[147,148]

$$\gamma_0^s = n_{WS}^{5/3}/(\varphi^* - 0.6)^2, \tag{16}$$

where γ_0^s is the surface energy of solid metals at $T = 0\,\mathrm{K}$, $n_{WS}^{5/3}$ is the electron density at the boundary of Wigner–Seitz cells, and φ^* is the electronegativity parameter. In the present case, formation of QWS significantly modifies the electron density near the Fermi energy,[70,149] which leads to a 2 ML period oscillation. Consequently, the surface energy should oscillate as well according to eq. (16), in agreement with the theory.[57]

An important factor influencing the measurement of adhesive force is the surface roughness, as discussed in the previous theoretical and experimental works.[150–155] When two rough surfaces are brought into contact, the real contact can happen only on the protruding points of the interface. That is, the real area of contact can be decreased as a result of surface roughness, which subsequently decreases the

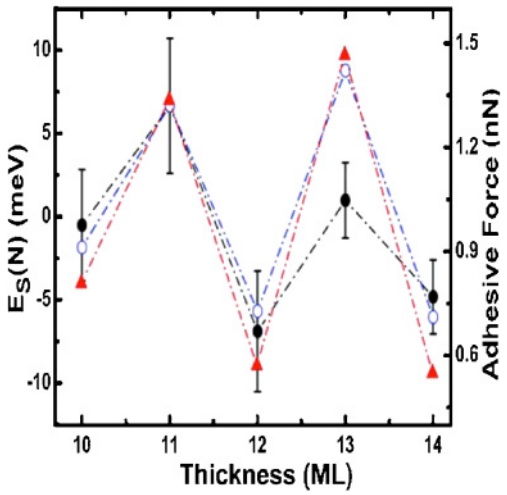

Fig. 26. (Color online) Calculated (open circles) and measured adhesive forces (filled circles) as a function of the thickness of Pb islands with respect to the wetting layer. The calculated relative surface energy vs thickness is also displayed (triangles).

adhesive force.[150,151] This is not the case here since the Pb island surfaces are atomically flat (Fig. 13). All these observations unambiguously reveal that the oscillatory adhesion forces originate from electronic effects associated with formation of QWS, which is a manifestation of strong QSE along the surface normal direction.

6. Conclusions and Perspectives

By growing atomically flat Pb films on Si(111) substrates in macroscopic scale, we are able to address the well-known 1D "particle in a box" problem and investigate various novel properties of such quasi-2D electronic systems induced by QSE. By using ARPES, STM/STS, AFM, and transport measurements, we have shown clearly how the formation of QWS could dramatically modulate the DOS(E_F) and thus regulate surface diffusion, superconducting transition temperature, perpendicular upper critical field, thermal expansion, LWF, and surface mechanical property (adhesion force).

Obviously, these studies are still preliminary, further studies are needed for better understanding the observed phenomena, and more areas need to be explored. As we showed above, the LWF is modified by QSE. Therefore, surface adsorption and chemical reactivity should be affected by QSE. Recently, we have carried out low temperature O_2 adsorptions on top of Pb wedge islands, and found both the adsorption and surface oxidation varies layer by layer and exhibit a persistent oscillation.[44] Similar results were reported recently on Mg films on W(110).[18,19] There are even less studies on friction, optical adsorption, reflectivity and son on.

The fundamental electronic structure of such quasi-2D electronic system is another important topic of interest for further study. It is still not fully understood how the QWS formed in the normal direction affect the in-plane motion of electrons in the film. The lateral effective mass m_{xy} dependence on film thickness was reported on Ag films.[94] More recently, the lateral bound states were observed in Pb and In thin films, a lateral electron confinement due to quantum enhancement of Coulomb interaction was proposed

to interpret the results.[156] However, the ARPES measurement suggests a strongly enhanced lateral electron localization (the lateral effective masses in Pb/Si(111) QWS are up to an order of magnitude larger than those from the bulk states or predicted by slab calculations), which was only observed in Pb/Si(111) but not in In/Si(111) system.[157]

According to the phase accumulation model,[2,3] the substrate and interface are crucial in the formation of QWS and affect film properties in a significant way as well. A recent study on Ag films on Ge(111) revealed that due to the coupling between the Ag valence electrons and the Ge substrate states, electronic states of Ag within the Ge fundamental gap formed fully confined quantum well states, while those outside the Ge gap formed partially confined quantum well resonances. The crossover from full to partial confinement was marked by a change in linewidth and a peak splitting.[158] By modifying the Si surface with different metals, the interface dependence of quantum wells was observed on Pb films.[159] Another work on the Ag films grown on 1D surface superstructure Si(111)-4 × 1-In reported that the lateral energy dispersion of QWS showed clear 1D anisotropy instead of the isotropic 2D free-electron-like behavior as expected for an isolated metal film.[160] Modification of interface structure provides another way for modulating the QSE.

Strain is inevitable in such systems. However, this is even less addressed. In an STS study on the Ag films grown on GaAs(110) surface, the s–p electronic band dispersion along the Γ–L direction was found shifted upward by about 190 meV compared to pure Ag(111) surfaces, which was attributed to the strain effect of the quasiperiodically modulated Ag film.[161] Unfortunately, it is very difficult to experimentally characterize the strain in a nano-meter thick thin film with atomic layer resolution.

In a more general sense, as our STS measurement of Pb thin films has shown, well-defined QWS are even visible at a thickness up to 43 ML, while the calculated oscillation for free Pb films disappears below 20 ML.[57] Obviously, at which point, for which property and by which reason the QSE is important await more delicate theoretical considerations, besides experimental efforts. The "particle in a box" is probably the simplest problem in quantum physics. However, in reality, the physics and effects resulted are actually much more complicated than expected, and new models/assumptions may need to develop. Nevertheless, the richness of the QSE induced phenomena observed even only in the Pb/Si(111) system, as discussed here, clearly suggests that this is one of most exciting interdisciplinary research areas in condensed matter physics, material science and chemistry, worth of study on more different materials by various technical approaches.

Acknowledgements

The authors would like to thank the present and previous members, Xucun Ma, Xi Chen, Hong Liu, Liying Ma, Ke He, Kang An, Yun Qi, Lili Wang, Tiezhu Han, Quantong Shen, Yingshuang Fu, Shuaihua Ji, Lin Tang, and Zelei Guan, of their research groups for the contributions to the results presented. The authors would also thank the fruitful collaborations with Enge Wang, Dongmin Chen, and Zhongxian Zhao (Institute of Physics), Feng Liu (University of Utah), Z. Q. Qiu (University of California at Berkeley), Shengbai Zhang (National Renewable Energy Laboratory), Qian Niu (University of Texas at Austin), X. C. Xie (Oklahoma State University), and S. C. Wu (Peking University). The projects were financially supported by NSFC, Ministry of Science and Technology of China and Chinese Academy of Sciences.

1) J.-J. Paggel, T. Miller, and T.-C. Chiang: Science **283** (1999) 1709.
2) T.-C. Chiang: Surf. Sci. Rep. **39** (2000) 181.
3) M. Milun, P. Pervan, and D.-P. Woodruff: Rep. Prog. Phys. **65** (2002) 99.
4) I.-B. Altfeder, K.-A. Matveev, and D.-M. Chen: Phys. Rev. Lett. **78** (1997) 2815.
5) I.-B. Altfeder and D.-M. Chen: Phys. Rev. Lett. **80** (1998) 4895.
6) I. Matsuda, T. Ohta, and H. W. Yeom: Phys. Rev. B **65** (2002) 085327.
7) L. Aballe, C. Rogero, and K. Horn: Phys. Rev. B **65** (2002) 125319.
8) R. K. Kawakami, E. Rotenberg, E. J. Escorcia-Aparicio, H. J. Choi, T. R. Cummins, J. G. Tobin, N. V. Smith, and Z. Q. Qiu: Phys. Rev. Lett. **80** (1998) 1754.
9) L. Aballe, C. Rogero, P. Kratzer, S. Gokhale, and K. Horn: Phys. Rev. Lett. **87** (2001) 156801.
10) M. Jałochowski and E. Bauer: Phys. Rev. B **38** (1988) 5272.
11) M. Jałochowski, M. Hoffman, and E. Bauer: Phys. Rev. Lett. **76** (1996) 4227.
12) B. G. Orr, H. M. Jaeger, and A. M. Goldman: Phys. Rev. Lett. **53** (1984) 2046.
13) H.-M. Jaeger, D.-B. Haviland, B.-G. Orr, and A.-M. Goldman: Phys. Rev. B **40** (1989) 182.
14) M. Jałochowski and E. Bauer: Phys. Rev. B **37** (1988) 8622.
15) M.-H. Upton, C.-M. Wei, M.-Y. Chou, T. Miller, and T.-C. Chiang: Phys. Rev. Lett. **93** (2004) 026802.
16) K. Morgenstern, E. Lægsgaard, and F. Besenbacher: Phys. Rev. Lett. **94** (2005) 166104.
17) E. Hüger and K. Osuch: J. Electron Spectrosc. Relat. Phenom. **141** (2004) 13.
18) L. Aballe, A. Barinov, A. Locatelli, S. Heun, and M. Kiskinova: Phys. Rev. Lett. **93** (2004) 196103.
19) N. Binggeli and M. Altarelli: Phys. Rev. Lett. **96** (2006) 036805.
20) M. Donath and D. H. Yu: Physica B **351** (2004) 319.
21) Y. Z. Wu, A. K. Schmid, M. S. Altman, X. F. Jin, and Z. Q. Qiu: Phys. Rev. Lett. **94** (2005) 027201.
22) L. Joly, L. Tati-Bismaths, and W. Weber: Phys. Rev. Lett. **97** (2006) 187404.
23) A. Varykhalov, A. M. Shikin, W. Gudat, P. Moras, C. Grazioli, C. Carbone, and O. Rader: Phys. Rev. Lett. **95** (2005) 247601.
24) Y. H. Yu, Y. Jiang, Z. Tang, Q. L. Guo, J. F. Jia, Q. K. Xue, K. H. Wu, and E. G. Wang: Phys. Rev. B **72** (2005) 205405.
25) M. Jałochowski, M. Strozak, and R. Zdyb: Phys. Rev. B **66** (2002) 205417.
26) T. Nozaki, N. Tezuka, and K. Inomata: Phys. Rev. Lett. **96** (2006) 027208.
27) W.-B. Su, S.-H. Chang, W.-B. Jian, C.-S. Chang, L.-J. Chen, and T.-T. Tsong: Phys. Rev. Lett. **86** (2001) 5116.
28) V. Yeh, L. Berbil-Bautista, C.-Z. Wang, K.-M. Ho, and M.-C. Tringides: Phys. Rev. Lett. **85** (2000) 5158.
29) M. Hupalo and M.-C. Tringides: Phys. Rev. B **65** (2002) 115406.
30) K. Budde, E. Abram, V. Yeh, and M.-C. Tringides: Phys. Rev. B **61** (2000) R10602.
31) A. Mans, J.-H. Dil, A. R. H. F. Ettema, and H.-H. Weitering: Phys. Rev. B **66** (2002) 195410.
32) P. Czoschke, H. Hong, L. Basile, and T.-C. Chiang: Phys. Rev. Lett. **93** (2004) 036103.
33) T.-C. Chiang: Chin. J. Phys. **43** (2005) 154.
34) D. A. Ricci, T. Miller, and T.-C. Chiang: Phys. Rev. Lett. **95** (2005) 266101.
35) F. Calleja, M. C. G. Passeggi, Jr., J. J. Hinarejos, A. L. Vázquez de Parga, and R. Miranda: Phys. Rev. Lett. **97** (2006) 186104.
36) Y. Guo, Y.-F. Zhang, X.-Y. Bao, T.-Z. Han, Z. Tang, L.-X. Zhang, W.-G. Zhu, E.-G. Wang, Q. Niu, Z.-Q. Qiu, J.-F. Jia, Z.-X. Zhao, and

Q.-K. Xue: Science **306** (2004) 1915.
37) T. C. Chiang: Science **306** (2004) 1900.
38) Y.-F. Zhang, J.-F. Jia, T.-Z. Han, Z. Tang, X.-C. Ma, and Q.-K. Xue: Surf. Sci. **596** (2005) L331.
39) S. C. Li, X. C. Ma, J. F. Jia, Y. F. Zhang, D.-M. Chen, Q. Niu, F. Liu, P. S. Weiss, and Q. K. Xue: Phys. Rev. B **74** (2006) 075410.
40) X.-Y. Bao, Y.-F. Zhang, Y. P. Wang, J. F. Jia, Q.-K. Xue, X. C. Xie, and Z.-X. Zhao: Phys. Rev. Lett. **95** (2005) 247005.
41) Y.-F. Zhang, J.-F. Jia, Z. Tang, T. Z. Han, Q. T. Shen, Y. Guo, Q. K. Xue, K. Xun, and S. C. Wu: Appl. Phys. Lett. **90** (2007) 093120.
42) T.-Z. Han, G.-C. Dong, Q.-T. Shen, Y.-F. Zhang, J.-F. Jia, and Q.-K. Xue: Appl. Phys. Lett. **89** (2006) 183109.
43) Y. Qi, X. C. Ma, P. Jiang, S. H. Ji, Y. S. Fu, J. F. Jia, Q. K. Xue, and S. B. Zhang: Appl. Phys. Lett. **90** (2007) 013109.
44) L. Y. Ma, L. Tang, Z. L. Guan, K. He, K. An, X. C. Ma, J. F. Jia, Q. K. Xue, Y. Han, S. Huang, and F. Liu: Phys. Rev. Lett. **97** (2006) 266102.
45) S.-C. Li, J.-F. Jia, R.-F. Dou, Q.-K. Xue, I. G. Batyrev, and S. B. Zhang: Phys. Rev. Lett. **93** (2004) 116103.
46) A. R. Smith, K.-J. Chao, Q. Niu, and C.-K. Shih: Science **273** (1996) 226.
47) L. Huang, S.-J. Chey, and J.-H. Weaver: Surf. Sci. **416** (1998) L1101.
48) L. Gavioli, K.-R. Kimberlin, M.-C. Tringides, J.-F. Wendelken, and Z.-Y. Zhang: Phys. Rev. Lett. **82** (1999) 129.
49) H. Hong, C.-M. Wei, M.-Y. Chou, Z. Wu, L. Basile, H. Chen, M. Holt, and T.-C. Chiang: Phys. Rev. Lett. **90** (2003) 076104.
50) C.-S. Jiang, H.-B. Yu, C.-K. Shih, and Ph. Ebert: Surf. Sci. **518** (2002) 63.
51) H. Liu, Y.-F. Zhang, D.-Y. Wang, M.-H. Pan, J.-F. Jia, and Q.-K. Xue: Surf. Sci. **571** (2004) 5.
52) Z.-Y. Zhang: Surf. Sci. **571** (2004) 1.
53) Z.-Y. Zhang, Q. Niu, and C.-K. Shih: Phys. Rev. Lett. **80** (1998) 5381.
54) Z. G. Suo and Z. Y. Zhang: Phys. Rev. B **58** (1998) 5116.
55) H. Okamoto, D.-M. Chen, and T. Yamada: Phys. Rev. Lett. **89** (2002) 256101.
56) C.-S. Jiang, S.-C. Li, H.-B. Yu, D. Eom, X.-D. Wang, Ph. Ebert, J.-F. Jia, Q.-K. Xue, and C.-K. Shih: Phys. Rev. Lett. **92** (2004) 106104.
57) C. M. Wei and M. Y. Chou: Phys. Rev. B **66** (2002) 233408.
58) *Surface and Diffusion: Atomostic and Collective Processes*, ed. M. C. Tringides (Plenum, New York, 1997).
59) Y. W. Mo, J. Kleiner, M. B. Webb, and M. G. Lagally: Phys. Rev. Lett. **66** (1991) 1998.
60) F. Liu and M. G. Lagally: in *The Chemical Physics of Solid Surfaces*, ed. D. A. King and D. P. Woodruff (Elsevier, 1997) Vol. 8, p. 258.
61) J. A. Venables: Philos. Mag. **27** (1973) 697.
62) G. Kresse and J. Hafner: Phys. Rev. B **47** (1993) R558.
63) Vinenna *ab initio* simulation package, Technische Universität Wien, 1999.
64) Y. Han and F. Liu: unpublished.
65) T.-L. Chan, C. Z. Wang, M. Hupalo, M. C. Tringides, and K. M. Ho: Phys. Rev. Lett. **96** (2006) 226102.
66) Y.-F. Zhang, J.-F. Jia, T.-Z. Han, Z. Tang, Q.-T. Shen, Y. Guo, and Q.-K. Xue: Phys. Rev. Lett. **95** (2005) 096802.
67) J.-R. Anderson and A.-V. Gould: Phys. Rev. **139** (1965) A1459.
68) M. Jałochowski, H. Knoppe, G. Lilienkamp, and E. Bauer: Phys. Rev. B **46** (1992) 4693.
69) J.-C. Boettger, J.-R. Smith, U. Birkenheuer, N. Rosch, S.-B. Trickey, J.-R. Sabin, and S.-P. Apell: J. Phys.: Condens. Matter **10** (1998) 893.
70) F. K. Schulte: Surf. Sci. **55** (1976) 427.
71) M. Breitholtz, T. Kihlgren, S.-A. Lindgren, and L. Wallden: Phys. Rev. B **67** (2003) 235416.
72) C. J. Fall, N. Binggeli, and A. Baldereschi: Phys. Rev. Lett. **88** (2002) 156802.
73) K. Besocke, B. Krahl-Urban, and H. Wangner: Surf. Sci. **68** (1977) 39.
74) E. Ogando, N. Zabala, E. V. Chulkov, and M. J. Puska: Phys. Rev. B **69** (2004) 153410.
75) P. J. Feibelman: Phys. Rev. B **27** (1983) 1991.
76) S. Ciraci and I. P. Batra: Phys. Rev. B **33** (1986) 4294.
77) J. C. Boettger and S. B. Trickey: Phys. Rev. B **45** (1992) 1363.
78) A. K. Ray and J. C. Boettger: Phys. Rev. B **70** (2004) 085418.
79) J. J. Paggel, C. M. Wei, D. A. Luh, T. Miller, and T. C. Chiang: Phys. Rev. B **66** (2002) 233403.
80) J. Kupers, K. Wandelt, and G. Ertl: Phys. Rev. Lett. **43** (1979) 928.
81) R. Fischer, S. Schuppler, N. Fischer, Th. Fauster, and W. Steinmann: Phys. Rev. Lett. **70** (1993) 654.
82) Y. Martin, D. W. Abraham, and H. K. Wichramasinghe: Appl. Phys. Lett. **52** (1988) 1103.
83) J. F. Jia, K. Inoue, Y. Hasegawa, W. S. Yang, and Y. Sakurai: Phys. Rev. B **58** (1998) 1193.
84) Y. Hasegawa, J. F. Jia, K. Inoue, A. Sakai, and T. Sakurai: Surf. Sci. **386** (1997) 328.
85) G. Binnig and H. Rohrer: Surf. Sci. **126** (1983) 236.
86) J. F. Jia, K. Inoue, Y. Hasegawa, W. S. Yang, and T. Sakurai: J. Vac. Sci. Technol. B **15** (1997) 1861.
87) B. Allen and R.-C. Dynes: Phys. Rev. B **12** (1975) 905.
88) A. Crottini, D. Cvetko, L. Floreano, R. Gotter, A. Morgante, and F. Tommasini: Phys. Rev. Lett. **79** (1997) 1527.
89) B.-A. McDougall, T. Balasubramanian, and E. Jensen: Phys. Rev. B **51** (1995) 13891.
90) T. Balasubramanian, E. Jensen, X.-L. Wu, and S.-L. Hulbert: Phys. Rev. B **57** (1998) R6866.
91) P. Hofmann, Y.-Q. Cai, C. Grütter, and J.-H. Bilgram: Phys. Rev. Lett. **81** (1998) 1670.
92) K. Takahashi, A. Tanaka, H. Sasaki, W. Gondo, S. Suzuki, and S. Sato: Phys. Rev. B **60** (1999) 8748.
93) E. Rotenberg, J. Schaefer, and S.-D. Kevan: Phys. Rev. Lett. **84** (2000) 2925.
94) M. Kralj, A. Siber, P. Pervan, M. Milun, T. Valla, P.-D. Jonson, and D.-P. Woodruff: Phys. Rev. B **64** (2001) 085411.
95) D.-A. Luh, T. Miller, J.-J. Paggel, and T.-C. Chiang: Phys. Rev. Lett. **88** (2002) 256802.
96) S. Mathias, M. Wiesenmayer, M. Aeschlimann, and M. Bauer: Phys. Rev. Lett. **97** (2006) 236809.
97) Y.-F. Zhang, J.-F. Jia, T.-Z. Han, Z. Tang, Q.-T. Shen, Y. Guo, and Q.-K. Xue: Chin. Phys. **14** (2005) 1910.
98) J. J. Paggel, T. Miller, and T.-C. Chiang: Phys. Rev. Lett. **83** (1999) 1415.
99) R. Paniago, R. Matzdorf, G. Meister, and A. Goldman: Surf. Sci. **336** (1995) 113.
100) B. J. Hinch, C. Koziol, J. P. Toennies, and G. Zhang: Vacuum **42** (1991) 309.
101) B. J. Hinch, C. Koziol, J. P. Toennies, and G. Zhang: Europhys. Lett. **10** (1989) 341.
102) W. J. Skocpol and M. Tinkham: Rep. Prog. Phys. **38** (1975) 1049.
103) J. Bardeen and J. R. Schrieffer: *Recent Developments in Superconductivity* (North-Holland, Amsterdam, 1991).
104) D. B. Haviland, Y. Liu, and A. M. Goldman: Phys. Rev. Lett. **62** (1989) 2180.
105) H. M. Jaeger, D. B. Haviland, B. G. Orr, and A. M. Goldman: Phys. Rev. B **40** (1989) 182.
106) J. M. Blatt and C. J. Thompson: Phys. Rev. Lett. **10** (1963) 332.
107) M. Yu, M. Strongin, and A. Paskin: Phys. Rev. B **14** (1976) 996.
108) A. Paskin and M. Strongin: Phys. Rev. Lett. **55** (1985) 139.
109) A. Frydman: Physica C **391** (2003) 189.
110) O. Pfennigstorf, A. Petkova, H. L. Guenter, and M. Henzler: Phys. Rev. B **65** (2002) 045412.
111) For the *ex situ* transport measurements, ~4 ML Au was deposited on the clean Pb thin films in the MBE chamber to avoid air contamination. The Au film grows also in layer-by-layer mode, and the surface morphology after Au deposition, as shown by our STM data, is essentially the same to that of the Pb film shown in the Figure. The critical transition temperature T_c at zero magnetic field extrapolated from the H_{c2}–T curve shows the same oscillatory behavior as the T_c in the R–T measurement. The results from the magnetic and resistance measurements are consistent so that the effects from the Au cover layer are eliminated.
112) M. Jałochowski and E. Bauer: Phys. Rev. B **38** (1988) 5272.
113) M. Jałochowski, E. Bauer, H. Knoppe, and G. Lilienkamp: Phys. Rev. B **45** (1992) 13607.
114) M. Tinkham: Phys. Rev. **129** (1963) 2413.
115) D. Saint-James and P. G. Gennes: Phys. Lett. **7** (1963) 306.
116) G. D. Cody and R. E. Miller: Phys. Rev. Lett. **16** (1966) 697.
117) G. D. Cody and R. E. Miller: Phys. Rev. **173** (1968) 481.
118) G. D. Cody and R. E. Miller: Phys. Rev. B **5** (1972) 1834.

119) Y. Bruynseraede, K. Temst, E. Osquiguil, C. van Haesendonck, A. Gilabert, and I. K. Schuller: Phys. Scr. **T42** (1992) 37.
120) M. V. Sadovskii: *Superconductivity and Localization* (World Scientific, Singapore, 2000).
121) P. G. de Gennes: *Superconductivity of Metals and Alloys* (W. A. Benjamin, New York, 1996).
122) M. Tinkham: *Introduction to Superconductivity* (McGraw-Hill, New York, 1996) 2nd ed.
123) N. Trivedi and N. W. Ashcroft: Phys. Rev. B **38** (1988) 12298.
124) D. Calecki: Phys. Rev. B **42** (1990) 6906.
125) A. E. Meyerovich and I. V. Ponomarev: Phys. Rev. B **65** (2002) 155413.
126) A. E. Meyerovich and I. V. Ponomarev: Phys. Rev. B **67** (2003) 165411.
127) A. E. Koshelev and A. A. Golubov: Phys. Rev. Lett. **90** (2003) 177002.
128) A. Gurevich: Phys. Rev. B **67** (2003) 184515.
129) D. Eom, S. Qin, M. Y. Chou, and C. K. Shih: Phys. Rev. Lett. **96** (2006) 027005.
130) M. M. Ozer, J. R. Thompson, and H. H. Weitering: Nat. Phys. **2** (2006) 173.
131) M. M. Özer, J. R. Thompson, and H. H. Weitering: Phys. Rev. B **74** (2006) 235427.
132) Z. Gahr and K. Heinz: *Microstructure and Wear of Materials* (Elsevier, Amsterdam/New York, 1987).
133) Y. Li and D. Y. Li: J. Appl. Phys. **95** (2004) 7961.
134) B. Bhushan: *Handbook of Micro/Nano Tribology* (CRC Press, Boca Raton, 1995).
135) D. H. Buckley: Wear **20** (1972) 89.
136) D. Y. Li and W. Li: Appl. Phys. Lett. **79** (2001) 4337.
137) Y. Li and D. Y. Li: J. Appl. Phys. **95** (2004) 7961.
138) Y. Li and D. Y. Li: Wear **259** (2005) 1432.
139) H.-Y. Nie, M. J. Walzak, B. Berno, and N. S. McIntyre: Appl. Surf. Sci. **144–145** (1999) 627.
140) P. B. Merrill and S. S. Perry: Surf. Sci. **418** (1998) 342.
141) A. Dayo, W. Alnasrallah, and J. Krim: Phys. Rev. Lett. **80** (1998) 1690.
142) J. N. Israelachvili: *Intermolecular and Surface Forces* (Academic Press, London, 1985).
143) Y. Han, J. Y. Zhu, F. Liu, S. C. Li, J. F. Jia, and Q. K. Xue: Phys. Rev. Lett. **93** (2004) 106102.
144) B. Bhushan: Wear **225–229** (1999) 465.
145) K. L. Johnson, K. Kendall, and A. D. Roberts: Proc. R. Soc. London, Ser. A **324** (1971) 301.
146) H. L. Skriver and N. M. Rosengaard: Phys. Rev. B **46** (1992) 7157.
147) A. R. Miedema and R. Boom: Z. Metallkd. **69** (1978) 183.
148) A. R. Miedema: Z. Metallkd. **69** (1978) 287.
149) J. Braun and J. P. Toennies: Surf. Sci. **384** (1997) L858.
150) Y. I. Rabinovich, J. J. Adler, A. Ata, R. K. Singh, and B. M. Moudgil: J. Colloid Interface Sci. **232** (2000) 10.
151) Y. I. Rabinovich, J. J. Adler, A. Ata, R. K. Singh, and B. M. Moudgil: J. Colloid Interface Sci. **232** (2000) 17.
152) H.-J. Butt, B. Cappella, and M. Kappl: Surf. Sci. Rep. **59** (2005) 1.
153) K. Cooper, A. Gupta, and S. Beaudoin: J. Colloid Interface Sci. **234** (2001) 284.
154) B. J. Briscoe and S. S. Panesar: J. Phys. D **25** (1992) A20.
155) S. Zilberman and B. N. J. Persson: J. Chem. Phys. **118** (2003) 6473.
156) I. B. Altfeder, X. Liang, T. Yamada, D. M. Chen, and V. Narayanamurti: Phys. Rev. Lett. **92** (2004) 226404.
157) J. H. Dil, J. W. Kim, Th. Kampen, K. Horn, and A. R. H. F. Ettema: Phys. Rev. B **73** (2006) 161308.
158) S.-J. Tang, L. Basile, T. Miller, and T.-C. Chiang: Phys. Rev. Lett. **93** (2004) 216804.
159) D. A. Ricci, T. Miller, and T.-C. Chiang: Phys. Rev. Lett. **93** (2004) 136801.
160) N. Nagamura, I. Matsuda, N. Miyata, T. Hirahara, S. Hasegawa, and T. Uchihashi: Phys. Rev. Lett. **96** (2006) 256801.
161) C.-S. Jiang, H.-B. Yu, X.-D. Wang, C.-K. Shih, and Ph. Ebert: Phys. Rev. B **64** (2001) 235410.

Jin-Feng Jia was born in Jiangsu Province, China in 1966. He obtained his B. Sc. (1987) and D. Sc. (1992) in physics from Peking University. He was an associate professor (1996–2001) at Department of Physics, Peking University, a professor (1991–2006) at Institute of Physics, Chinese Academy of Sciences. Since 2006, he has been a professor at Department of Physics, Tsinghua University. He has worked on surface physics using LEED, UHV-STM, ARPES, AES, EELS, SMOKE and etc. His research is now focused on growth of nanostructures on surfaces and characterization of their special properties.

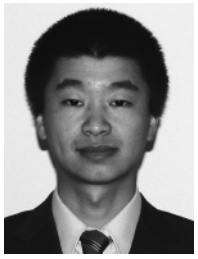

Shao-Chun Li was born in Heilongjiang Province, China in 1977. He obtained his B.S. in physics (1999) from Peking University, China, and Ph. D. (2004) in condensed matter physics from Institute of Physics, Chinese Academy of Sciences. He was a Postdoctoral Fellow in Department of Chemistry, Pennsylvania State University from 2005 to 2006, and he is presently a postdoctoral researcher at Pacific Northwest National Laboratory (from 2006), USA. He has worked on exploring the quantum confinement in metal/semiconductor system and nanostructure manipulations, chemical reactions on metal surfaces by using scanning tunneling microscopy and scanning tunneling spectroscopy. His present research interest is focused on the catalytic reactions on metal oxide surfaces.

Yan-Feng Zhang was born in Henan Province, China in 1976. She obtained her B. Sc. (1999), M. Sc. (2002) degrees from Zhengzhou University, and her D. Sc. (2005) degree from Institute of Physics, Chinese Academy of Sciences. Now, she is working as a postdoctoral fellowship at the Institute of Multidisciplinary Research for Advanced Materials, Tohoku University, Japan (from 2006). She has worked on the preparation of atomically flat metal thin films on semiconductor substrate, and investigation the quantum size effects (QSE) induced novel physical properties such as the superconductivity, thermal expansion, electron phonon coupling and so on. Her research is now focused on the investigation of metal-organic coordination interactions, and related novel physical properties of single organic molecules and single magnetic atoms.

Qi-kun Xue was born in Shan-Dong Province, China in 1963. He obtained his B. Sc. (1984) from Shan-Dong University, M. Sc. (1990) and D. Sc. (1994) degrees from Institute of Physics, Chinese Academy of Sciences. He was a research associate (1994–1999) at Institute for Materials Research, Tohoku University, Japan. He became a professor and the director (1999–2006) of the State Key Laboratory for Surface Physics, Institute of Physics, Chinese Academy of Sciences. He was elected as the Member of the Chinese Academy of Sciences in 2005. Since 2006, he has been a "Cheung Kong" Professor of Material Physics at Department of Physics, Tsinghua University. When he worked at Tohoku University, his research focused on determination of surface atomic structures of conventional III–V semiconductor surface reconstructions, and atomic scale understanding of growth kinetics of InAs/GaAs, GaN/SiC, and fullerene/GaAs. His current interest is the molecular beam epitaxy growth and atomic-level control of semiconductor/metal thin films, and the novel physical/chemical properties and quantum effects in nanostructures (clusters, quantum dots/wires etc.) using scanning tunneling microscopy, angle-resolved photoemission spectroscopy, and surface magnetic-optical Kerr effect.